RSC Advances

ROYAL SOCIETY OF CHEMISTRY

PAPER

View Article Online
View Journal | View Issue

Cite this: *RSC Adv.*, 2026, **16**, 23500

Dynamic light scattering-assisted design of an optimized NiS–ZnS nanocomposite for efficient photocatalytic dye degradation: experimental and theoretical insights

Muhammad Younas Afzal,[ab] Muhammad Bilal,*[b] Muhammad Asif,[bc] Saeed Rehman,[d] Jamshaid Hussain,[e] Qing Liu,[f] Hamza Khan,[a] Nadia Riaz,[b] Farooq Ahmad,[g] Muhammad Tahir Amin*[h] and Ahson Jabbar Shaikh*[a]

Received 3rd March 2026
Accepted 12th April 2026

DOI: 10.1039/d6ra01846g

rsc.li/rsc-advances

Industrial dye pollutants demand efficient photocatalysts for sustainable wastewater treatment. Here, we report the synthesis of pure NiS, ZnS, and a negatively charged, optimized NiS–ZnS nanocomposite (NC) *via* coprecipitation, with their size and stability controlled by adjusting the precursor ratio, pH, temperature, stabilizer concentration, and reactant addition rate. Dynamic light scattering (DLS) analysis was used to monitor hydrodynamic radius (H_R), ζ-potential, and polydispersity index (PdI), providing real-time insights into dye adsorption, degradation dynamics, and salt–nanocomposite interactions. Optimized NiS : ZnS 50 : 50 nanocomposite showed high colloidal stability, achieved 98% crystal violet (CV) degradation within 60 min under visible light, outperforming other cationic dyes while being less effective for anionic dyes. Characterization of the NiS–ZnS NC (UV-Vis spectroscopy, PL spectroscopy, XRD, FTIR spectroscopy, EDX, XPS, SEM, TEM, TGA, and BET analysis) confirmed its visible light activity, suppressed charge recombination rate, successful synthesis, agglomerated nature, thermal stability, and mesoporous structure. Density functional theory (DFT), density of states (DOS), and electrostatic potential analyses showed bandgap narrowing, favorable dye binding, and efficient charge transfer supported by strong interaction energies. Salt studies revealed surface-charge modulation and radical pathways, with $NaNO_3$ enhancing the degradation *via* $^{\bullet}OH$ generation, while $CaCl_2$ and $AgNO_3$ suppressed the degradation activity. LC-MS and total organic carbon (TOC) analysis confirmed dye mineralization and reduced toxicity, with seed germination assays verifying the biocompatibility of the NiS–ZnS NC. The generation of the reactive species $^{\bullet}OH$ and $^{\bullet}O_2^-$ was confirmed using electron spin resonance (EPR) spectroscopy and quencher experiments. This integrated experimental-computational approach establishes NC as a robust, charge-engineered photocatalyst for visible-light-driven dye remediation.

Introduction

Water is the most essential resource for life and ecosystem sustainability, yet its quality is increasingly threatened by diverse anthropogenic pollution sources.[1–3] Among emerging contaminants, synthetic dyes released from textile, leather, paper, and printing industries are of particular concern because of their chemical stability and resistance to natural degradation.[2,4] Both cationic dyes (*e.g.*, crystal violet, malachite green, and methylene blue) and anionic dyes (*e.g.*, reactive black 5, orange II, and reactive orange 16) persist in aquatic systems, posing serious risks to ecosystems and human health. Their intense coloration reduces light penetration and disrupts photosynthesis, and many are toxic, mutagenic, or carcinogenic. Because of their persistence and hazardous effects, dye-contaminated wastewater has become a pressing global challenge for maintaining environmental sustainability and public health.[5]

---

[a] Department of Chemistry, COMSATS University Islamabad, Abbottabad Campus, KPK, Abbottabad – 22060, Pakistan. E-mail: ahson@cuiatd.edu.pk
[b] Department of Environmental Sciences, COMSATS University Islamabad, Abbottabad Campus, KPK, Abbottabad – 22060, Pakistan. E-mail: mbilal@cuiatd.edu.pk
[c] Graduate School of Science and Technology, University of Tsukuba, 1-1-1 Tennodai, Tsukuba, Ibaraki, 305–8573, Japan
[d] School of Environment and Resources, Laboratory of Solid Waste Treatment and Resource Recycle, Southwest University of Science and Technology, Mianyang, 621010, China
[e] Department of Biotechnology, COMSATS University Islamabad, Abbottabad Campus, KPK, Abbottabad – 22060, Pakistan
[f] College of Chemical Engineering, Nanjing Tech University, NO. 30 Puzhu South Road(S), Nanjing 211816, PR China
[g] Department of Chemical and Materials Engineering, Northern Border University, Arar, 91431, Kingdom of Saudi Arabia
[h] Department of Civil and Environmental Engineering, College of Engineering, King Faisal University, Al-Ahsa 31982, Saudi Arabia. E-mail: mqdir@kfu.edu.sa

Crystal violet (CV), a cationic triphenylmethane dye, exemplifies this problem. It is extensively used in industrial and commercial applications, including textiles, paper, cosmetics, detergents, fertilizers, and leather processing, making it one of the most prevalent dyes in wastewater streams.[6] CV is also a known carcinogen, capable of inducing chromosomal damages and severe cellular abnormalities, and its release into aquatic environments has been linked to toxicity in microorganisms, plants, and aquatic organisms.[7,8] Moreover, its highly aromatic structure and chemical stability render it resistant to natural degradation. Owing to these characteristics, CV is frequently used as a model pollutant in photocatalytic studies to quantify the efficacy of advanced materials in pollutant degradation and remediation.

Various conventional methods have been investigated for dye removal, including ion exchange,[9] precipitation, membrane separation,[10] and adsorption.[11] While these techniques can reduce dye concentrations, they are often limited by high operational costs, secondary waste generation, or incomplete pollutant removal, and they rarely achieve full mineralization. Photocatalytic degradation (PCD), an advanced oxidation process,[12] has emerged as a more sustainable alternative. By generating electron–hole (e^-/h^+) pairs under light irradiation, semiconductor photocatalysts produce reactive oxygen species (ROS), such as superoxide ($O_2^{\bullet-}$) and hydroxyl radicals ($^{\bullet}OH$),[13] which oxidize organic pollutants into non-toxic end products (CO_2 and H_2O).[14,15] PCD is a simple, energy-efficient, and environmentally friendly process, making it highly attractive for large-scale wastewater treatment.[16]

A wide range of semiconductors, including sulfides (NiS, ZnS, CuS, and SnS), oxides (TiO_2, ZnO, and MnO_2), nanocomposites (*e.g.*, ZnS/PbS and MoS_2/SnS_2@AC),[17,18] and nanohybrids (*e.g.*, GO/ZnS,[19] Ag–Bi_2O_3/rGO composites,[20] S-doped-C_3N_4/ZnCdS,[21] and sulfur-doped g-C_3N_4/rGO[22]), have been explored for photocatalysis. Zinc sulfide (ZnS) and nickel sulfide (NiS) nanoparticles are versatile materials with high potential for water treatment and advanced oxidation processes (AOPs) for pollution remediation.[23]

Zinc sulfide (ZnS), an n-type semiconductor, is notable for its low cost, high stability, and visible light activity.[24] Its suspension stability, supported by a high surface charge and low hydrodynamic radius (H_R), makes it attractive for aqueous applications. However, ZnS suffers from rapid charge-carrier recombination due to surface defects, as evidenced by its strong photoluminescence (PL) emission.[25] This recombination limits its photocatalytic performance. Studies have demonstrated that introducing dopants and developing heterostructures are promising strategies for suppressing charge-carrier recombination in ZnS-based systems. Notably, ZnS/ZnO heterostructures display enhanced charge-separation efficiency,[26] while Ni and Fe doping in ZnS reduces the photoluminescence intensity, signifying suppressed e^-/h^+ recombination and enhanced photocatalytic performance.[27,28] Similarly, ZnS/SnS heterostructures exhibit suppressed recombination,[29] and the CdS/ZnS–MoS_2 composite facilitates electron transfer from ZnS to MoS_2, further promoting charge separation.[30] These results suggest that coupling ZnS with a visible light-active electron acceptor is essential to inhibiting charge recombination and augmenting photocatalytic performance.

Nickel sulfide (NiS), a p-type semiconductor with a narrow bandgap, has been used as an efficient photosensitizer and electron acceptor.[31] Its incorporation can prolong charge-carrier lifetimes and enhance charge separation.[32] In our previous study, NiS nanoparticles exhibited visible light activity, high stability, and excellent recyclability for the photocatalytic degradation of reactive black 5 dye.[33] Therefore, coupling NiS with ZnS to construct a p-n heterojunction nanocomposite (NC) constitutes a rational design strategy to suppress charge-carrier recombination, enhance interfacial charge transfer, and increase the availability of active sites, thereby improving photocatalysis performance.[16,34,35]

This study reports the synthesis of pure NiS, ZnS, and an engineered optimized NiS–ZnS nanocomposite (NC) *via* a coprecipitation route.[36] The key novelty of this work lies in the utilization of dynamic light scattering (DLS) as both a design and mechanistic-investigation tool. Specifically, DLS parameters, including H_R, Zeta potential (ζ), and polydispersity index (PdI), were systematically optimized by tuning the precursor ratios, pH, temperature, stabilizer concentration, and reactant addition rate. This approach enabled precise control over the physicochemical properties of the NiS–ZnS NC, yielding stable nanocomposites with reduced H_R, appropriate surface charge, and uniform dispersion, thereby augmenting the effective surface area for pollutant degradation.[37]

Beyond the synthesis conditions, DLS was uniquely employed to monitor real-time fluctuations in H_R and ζ during dye adsorption and photocatalytic degradation, as well as in varying ionic environments. These measurements revealed the interaction between NiS–ZnS nanocomposites and the crystal violet dye, where variations in surface charge and an increase in H_R verify dye adsorption followed by subsequent degradation. This provides new insights into the nanoscale mechanisms governing dye degradation and indicates a direct correlation between dye–nanocomposite interactions and photocatalyst efficacy, which is rarely explored in photocatalysis research. Furthermore, the influence of inorganic cations (Na^+, Ag^+, and Ca^{2+}) and anions (Cl^-, SO_4^{2-}, and NO_3^-) on the nanocomposite behavior was systematically investigated through changes in H_R and surface charge, elucidating their role in dye adsorption and the photocatalytic degradation process, consistent with previous reports.[38,39]

To further support these experimental insights, complementary computational studies based on density functional theory (DFT) were performed to gain deeper insights into the electronic structure and interfacial interactions. HOMO–LUMO, density of states (DOS), electrostatic potential (ESP), and non-covalent interaction (NCI) analyses revealed bandgap narrowing, favorable crystal violet binding at multiple active sites, strong interaction energies, and enhanced charge transfer across the dye–nanocomposite interface. These theoretical insights are in excellent agreement with experimental observations, highlighting charge-carrier-recombination suppression, efficient radical generation, and superior dye degradation efficiencies.

Together, this integrated experimental–computational strategy establishes the NiS–ZnS composite as a robust, charge-engineered photocatalyst. By combining DLS-guided design with theoretical validation, this study not only describes an efficient material for visible light–driven dye remediation but also furnishes a generalizable framework for understanding and optimizing dye–nanocomposite interactions in photocatalytic wastewater treatment.

Experimental work

Materials

Nickel acetate tetrahydrate [$Ni(CH_3COO)_2 \cdot 4H_2O$], zinc acetate hexahydrate [$Zn(CH_3COO)_2 \cdot 6H_2O$], sodium sulfide ($Na_2S$), and polyvinyl alcohol (PVA); HCl and NaOH for pH control; inorganic salts, including NaCl, Na_2SO_4, $NaNO_3$, $AgNO_3$ and $CaCl_2$; and organic scavengers, including ethanol, isopropyl alcohol (IPA), butanol, ethylene diamine tetra acetic acid (EDTA) and ascorbic acid, were purchased from DaeJung Chemicals (Republic of Korea). Crystal violet (CV), malachite green (MG), methylene blue (MB), reactive black 5 (RB5), Orange II indicator, and reactive orange 16 dyes were purchased from Sigma-Aldrich (Germany). All chemicals were of analytical grade and used as received.

Preparation of stock solutions

0.5 M nickel and zinc acetate solutions and a 1 M Na_2S solution were prepared in distilled water. For salt effect studies, 0.1 M solutions of NaCl, $CaCl_2$, $NaNO_3$, Na_2SO_4, and $AgNO_3$ were prepared. Organic scavengers (ethanol, butanol, IPA, EDTA, and ascorbic acid) were also prepared at 0.1 M. No pH adjustments were made. Dye solutions were prepared by dissolving 1 g in 1 L of distilled water to make a 1000 mg L^{-1} solution. For the desired concentrations, the dilution factor was used. Among the dyes, the NiS–ZnS NC showed good interaction with crystal violet dye; consequently, this dye was chosen for further optimization and mechanistic studies.

Synthesis of the NiS and ZnS nanoparticles

NiS was synthesized by stirring nickel acetate (0.5 M) with 1% PVA at 60 °C, followed by dropwise addition of Na_2S (1 M, double volume). The mixture was stirred for 3 h, centrifuged, washed with ethanol/water, and dried at 100 °C. ZnS was synthesized under identical conditions at 25 °C. Both powders were ground before characterization (Fig. S1).

Synthesis of the NiS–ZnS nanocomposite

Equimolar solutions (0.5 M) of Ni and Zn acetates were mixed and treated with Na_2S (double volume) under stirring at 40 °C for 3 h. The precipitates were centrifuged, washed, and dried. For optimization, synthesis parameters, including precursor ratios (100 : 0–0 : 100), pH (3–9), temperature (20–80 °C), Na_2S addition time (0–20 min), and PVA concentration (0–2%), were systematically varied (Fig. S1).

Adsorption studies

Adsorption kinetics were studied using different initial CV concentrations (2–30 mg L^{-1}) and 0.2 g L^{-1} of the nanocomposite at room temperature. The mixture was stirred in the dark for 20 min, and samples were collected at 3-minutes intervals and analyzed spectrophotometrically. Adsorption studies were conducted to study the adsorption–desorption equilibrium of CV and its interactive role with the NiS–ZnS NC. The adsorbed quantity and adsorption percentage were calculated using eqn (1) and (2).[40]

$$q_t = \frac{(C_0 - C_t)V}{m} \tag{1}$$

$$\text{Adsorption }\% = \frac{(C_0 - C_t)}{C_0} \times 100 \tag{2}$$

where q_t = adsorption capacity at equilibrium (mg g^{-1}), C_0 = initial CV concentration (mg L^{-1}), C_t is the residual concentration after time t, V is the volume of solution (L), and m is the nanocomposite weight (g L^{-1}).

Photocatalytic studies

For dye degradation, 50 mL of the 20 mg L^{-1} CV solution was mixed with 0.2 g L^{-1} of the nanocomposite at pH 6.9 and stirred (300 rpm) in the dark for 20 min to establish the adsorption equilibrium. The solution was then irradiated for 60 min under a 500 W visible light source with a 30 798 l× intensity (Halogen lamp, Hi Luminar, Germany) at a distance of 25 cm.[41] 4 mL aliquots were withdrawn every 10 min for UV-Vis analysis at 576 nm. Effects of catalyst dosage (0.04–0.20 g L^{-1}), pH (2–12), initial dye concentration (2–30 mg L^{-1}), and recyclability (up to 7 cycles) were evaluated. Degradation efficiency and mineralization (TOC removal in mg L^{-1}) were calculated using eqn (3) and (4).[40,42] Photocatalytic degradation kinetic analysis was performed using pseudo-first order (PFO) and Langmuir–Hinshelwood models.[43] The degradation rate for various CV concentrations was calculated using (eqn (5)).[44] The L-H model (eqn (6))[43] describes the reaction rate (r_0) as a function of both adsorption and surface photocatalytic activity (K_c).

$$\text{Degradation }\% = \frac{C_0 - C_t}{C_0} \times 100 \tag{3}$$

$$\text{TOC removal}(\%) = \frac{\text{TOC}_0 - \text{TOC}_t}{\text{TOC}_0} \times 100 \tag{4}$$

$$\ln\left(\frac{C_0}{C_t}\right) = k_{\text{app}}t \tag{5}$$

$$\frac{1}{r_0} = \frac{1}{K_c} + \frac{1}{K_c K_{\text{ads}}} \times \frac{1}{[\text{CV}]_e} \tag{6}$$

In eqn (3) and (5), C_0 and C_t are the initial and final CV concentrations (mg L^{-1}), respectively, $[\text{CV}]_e$ represents the equilibrium concentration of crystal violet, and k_{app} represents the apparent degradation rate constant. In eqn (4), TOC_0 and TOC_t are the initial and final TOC of the dye solution in mg L^{-1}, respectively.[33] In eqn (6), r_0 is the initial degradation rate (mg

L^{-1} min), and K_c is the surface reaction rate constant (mg L^{-1} .min), which tells us about surface reactivity; K_{ads} is the adsorption equilibrium constant (L mg^{-1}), which reflects the dye-catalyst affinity (eqn (6)).[43]

To enable comparison with photon-flux-normalized metrics, it is important to note that the light intensity used in this study is reported in terms of lamp power and illuminance (lux), which do not directly provide the incident photon flux at the reactor. Therefore, the apparent quantum yield (AQY) could not be rigorously determined under the present experimental conditions. A quantitative AQY evaluation requires photon-flux measurements using chemical actinometry or calibrated radiometric techniques under monochromatic irradiation. In this work, photocatalytic performance is, thus, discussed in terms of degradation efficiency under fixed irradiation conditions.

Toxicity and salt/scavenger effects

The phytotoxicity of CV and treated solutions was tested using tomato seeds following ISO/DIS 15799 (1999). The effects of salts (0.1 M) and organic scavengers (0.1 M) on the photocatalytic activity were studied by monitoring CV degradation *via* UV-Vis spectroscopy. Control salt studies were performed by adding 10 mL of 0.1 M of each salt directly to the dye solution and stirring for 60 min without NC. EPR analysis was conducted using 20 mg L^{-1} of DMPO and TEMP for reactive species ($^{\bullet}OH$ and $^{\bullet}O_2^{-}$) generation.

Characterization

Optical properties were examined using UV-vis (Specord 200+) and fluorescence spectroscopy (PerkinElmer LS-45). Hydrodynamic size (H_R), zeta potential, and polydispersity index were determined *via* DLS (Malvern Zetasizer). Structural analysis was performed *via* XRD analysis (Bruker D8 Advance), and the crystallite size was confirmed using eqn (7) (ref. 45) and FTIR (PerkinElmer). Binding energies were calculated using XPS (XPS, AES430S, ANELVA, Japan). Morphology and elemental distribution were characterized by SEM-EDX (JEOL JSM-6510LV). Surface area and porosity were determined *via* BET (Nova-1000). Transmission electron microscopy (TEM) was employed to examine the morphology and microstructural features of the synthesized samples (TEM, FEI Talos F200X). Thermal stability and decomposition behavior were investigated using thermogravimetric analyses (TGA-STA 8000, PerkinElmer, USA). Electron paramagnetic resonance (EPR, Bruker EMXplus-6/1) spectroscopy was used to probe the unpaired electron species and defect states within the nanocomposite. The degradation intermediates and products were analyzed using liquid chromatography-mass spectrometry (LC-MS, AB Sciex, API4000), furnishing insights into the degradation pathway.

$$D = \frac{K\lambda}{\beta \cos \theta} \quad (7)$$

where D is the crystal size (nm), K is the Scherrer constant representing the particle shape with a value of 0.9, λ is the wavelength of X-ray (copper Kα radiation, $\lambda = 0.15406$ nm), θ indicates the diffraction angle, and β is the full width at half-maximum (FWHM) of the diffraction peak.[45]

DFT studies

In this study, ChemBioDraw Ultra 14.0 was used for drawing molecular structures, which were then modelled and visualized using Gauss View 6.0. All quantum chemical calculations were performed using the Gaussian 09W software package.[46] Geometry optimizations for dyes, metal sulfides, and their complexes were conducted using Density Functional Theory (DFT) with the B3LYP functional and the STO-3G basis set. For the Density of States (DOS) analysis, the Gauss Sum software was employed. Non-Covalent Interaction (NCI) and Reduced Density Gradient (RDG) analyses were carried out using the Multiwfn program and visualized through the VMD software. All computational resources and facilities used for this research were provided by COMSATS University Islamabad, Abbottabad Campus. The interaction energies for all optimized complexes were calculated using the standard interaction energy equation to assess the binding strength.

Results and discussions

Concentration optimization of the NiS–ZnS NC

The structural and colloidal properties of the NiS–ZnS NC were systematically optimized by tuning the precursor ratios, pH, temperature, time of addition (TOA) of Na_2S, and polyvinyl alcohol (PVA) concentration. Dynamic light scattering (DLS) and absorption studies were used to evaluate H_R, surface charge (ζ potential), and polydispersity index (PdI), which together define the nanocomposite stability and photocatalytic potential.

Precursor ratio

As shown in Fig. 1a and b, the NiS : ZnS ratio strongly influenced the size distribution and stability of the NCs. The 50 : 50 composition yielded smaller H_R values, a more homogeneous particle distribution, and higher stability compared to other compositions, and it was, therefore, selected for further optimization.

pH dependence

The role of the synthesis medium was probed across acidic, neutral, and alkaline conditions (Fig. 1d). At pH 5, the NC exhibited the lowest H_R, the highest stability,[47] and the narrowest size distribution, whereas destabilization occurred at extreme pH values. Under alkaline conditions (pH $\approx$ 9), amphoteric $Zn(OH)_2$ was converted into soluble zincate $[Zn(OH)_4]^{2-}$, while Ni(II) precipitated as $Ni(OH)_2$ or NiS, resulting in Ni-rich phases. At acidic pH ($\approx$2), sulfide protonation produced H_2S and dissolved metal sulfides,[48] leaving predominantly ZnS, consistent with the ZnS-like diffraction peaks. At near-neutral pH (6.5), both the NiS and ZnS peaks were observed (Fig. 1c), but with reduced stability compared to those at pH 5. Based on these results, pH 5 was chosen as the optimum condition for subsequent experiments.

Temperature optimization

Temperature strongly affected both H_R and ζ potential (Fig. 1f). At 20 °C, the lower H_R peak corresponded mainly to ZnS,

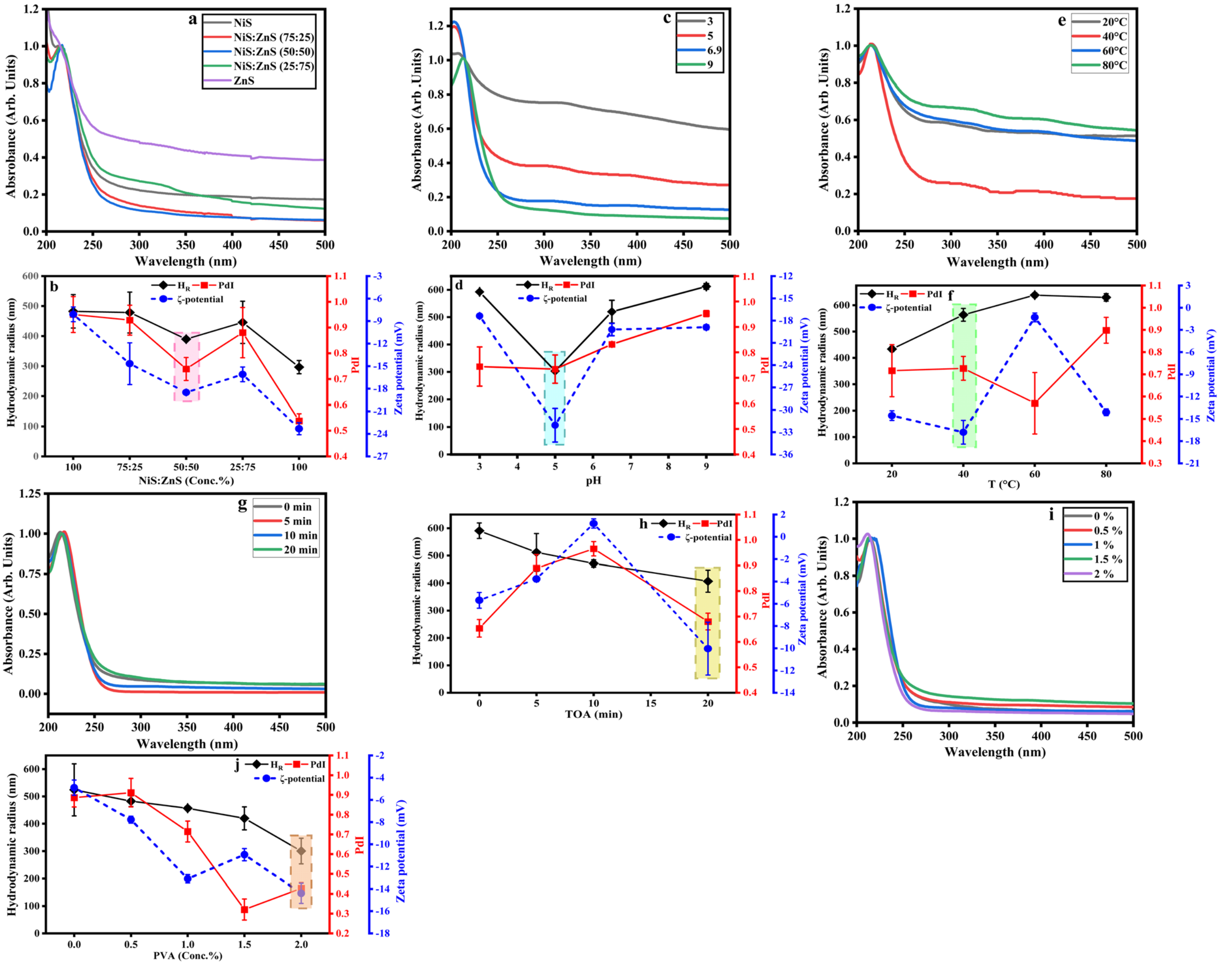

Fig. 1 Optimization of the NiS–ZnS NC. Concentration optimization: (a) UV-vis spectra; (b) H_R, ζ potential, and PdI (pH: 6.5, T: 20 °C, stirring speed: 500 rpm, TOA: 10 min, reaction time: 3 hours). pH optimization: (c) UV-vis spectra; (d) H_R, ζ potential, and PdI (precursor ratio (50 : 50), T: 20 °C). Temperature optimization: (e) UV-vis spectra; (f) H_R, ζ potential, and PdI (precursor ratio (50 : 50), pH: 5). Time of addition optimization: (g) UV-vis spectra; (h) H_R, ζ potential, and PdI (precursor ratio (50 : 50), pH: 5, T: 40 °C). PVA conc. (%) optimization: (i) UV-vis spectra; (j) H_R, ζ potential, and PdI (precursor ratio (50 : 50), pH: 5, T: 40 °C, TOA: 20 min).

indicating its dominance. With increasing temperature, the NiS contribution became more evident, particularly at 60 °C, where the NiS peak slightly predominated (Fig. 1e). A stabilized NC was achieved at 40 °C, characterized by a ζ potential of −18.3 ± 1.44 mV, attributed to the reduced collision frequency and slower nucleation-growth kinetics. Above 60 °C, rapid ion consumption led to accelerated nucleation and aggregation, producing larger clusters and reducing colloidal stability.[49] Consequently, stability declined at higher temperatures, consistent with earlier reports of temperature-driven aggregation in sulfide nanomaterials.[50] The PdI values generally increased with temperature, except at 60 °C, where transient stabilization by NiS suppressed broadening.

Time of addition (TOA)

The rate of Na_2S addition also influenced the NC characteristics, as depicted in (Fig. 1g and h). At pH 5 and 40 °C, gradual addition produced more uniform size distributions, whereas rapid addition caused irregular ion distributions, reflected in hyperchromic shifts (320–340 nm) and peak broadening.[51] Faster addition likely generated transient intermediate species, reducing the absorption intensity of the final product (Fig. 1g). At higher TOA, H_R decreased in line with an increase in the surface charge, while PdI decreased, indicating better homogeneity. These observations highlight the role of controlled nucleation in stabilizing sulfide nanostructures (Fig. 1h).[52]

Effect of the PVA concentration

PVA, used as a stabilizing agent, further enhanced dispersion (Fig. 1i). Increasing the PVA concentration led to higher absorption intensity, except at 1.5%, where aggregation was observed. At higher concentrations (>2%), interparticle coupling was suppressed, and the plasmon band shifted to shorter wavelengths, consistent with reduced electronic interactions between NCs (Fig. 1j).[53] The reduction in H_R was attributed to the formation of a polymeric shell around the NC surface, while PdI initially declined up to 1.5% PVA before increasing again, likely due to the viscosity effects in concentrated suspensions.[54] The final ζ potential reached −14.4 ± 0.9 mV at 2% PVA, indicating effective stabilization.[55]

Optimized nanocomposite

The combined parameter screening identified the optimum synthesis conditions as NiS : ZnS (50 : 50), pH 5, 40 °C, PVA concentration of 2%, and TOA of 20 min. Under these conditions, the NC achieved a hydrodynamic size of 300 ± 46.7 nm (Fig. S4) and PdI of 0.42 ± 0.20, compared to the size of 389.9 ± 7.1 nm and the PdI of 0.95 ± 0.07 for non-optimized samples. These results confirm superior colloidal stability, reduced aggregation, and enhanced surface area under the optimized synthesis conditions. Such characteristics are expected to improve photocatalytic activity by promoting efficient dye-catalyst interactions and prolonging catalyst lifetime.

SEM images and BET specific surface area of the NiS–ZnS NC, and XRD spectra of pure NiS, ZnS, and the NiS–ZnS NC

SEM images of NC are measured at different resolutions, revealing irregular morphologies with fracture edges and highly agglomerated fine particles with rough surfaces (Fig. 2a and b). Although the two nanomaterials are not distinctly visible in the structure, the electron images (Fig. S2) indicate that ZnS is uniformly embedded within the NiS matrix. This uniform distribution is further supported by the EDX data (Fig. S2), which confirms consistent elemental composition throughout the material.

The Brunauer–Emmett–Teller (BET) analysis revealed a specific surface area of 65.3 m^2 g^{-1} for the NiS–ZnS NC, measured at 77 K using 20 relative pressure (P/P_0) points in the range of 0–1. Pore-size distribution, determined by density functional theory (DFT), indicated a total pore volume of 0.141 cm^3 g^{-1} and an average pore diameter of 0.563 nm (Fig. 2e). The nitrogen adsorption–desorption isotherm (Fig. 2d) displays a typical type-IV profile with a pronounced H3-type hysteresis loop, characteristic of mesoporous materials.[56] The gradual increase in adsorption capacity with relative pressure, together with the hysteresis observed in the desorption branch, reflects the capillary condensation within mesopores. These textural features confirm a mesoporous structure with high surface area, offering abundant active sites and efficient mass transfer. Such architecture enhances light interaction and dye diffusion, thereby promoting the photocatalytic and adsorption performance of the material toward crystal violet.

XRD patterns of pure NiS, ZnS NPs, and the NiS–ZnS NC (Fig. 2f). Two phases for nickel sulfide were detected, with orthorhombic Ni_7S_6 being the dominant phase, using the JCPDS Card # 00-024-1021, showing nine major diffraction peaks located at 2θ values of 19.44°, 20.72°, 22.19°, 27.12°, 30.97°, 32.07°, 38.29°, 39.57°, and 49.08°, corresponding to the (040), (032), (042), (004), (131), (044), (133), and (026) planes, respectively. Few peaks of

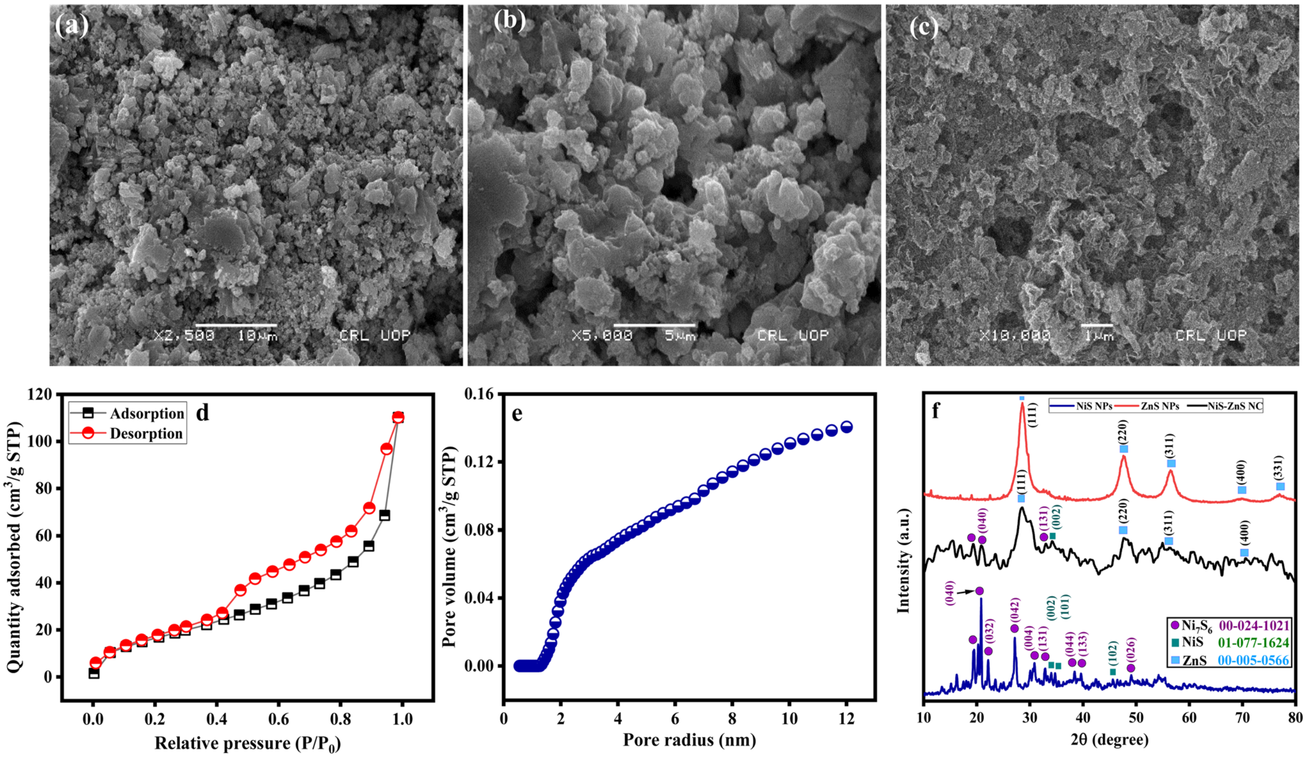

Fig. 2 SEM micrographs at different resolutions: (a) 10 µm, (b) 5 µm, and (c) 1 µm. (d) BET specific surface area using N_2 adsorption–desorption isotherms; (e) pore volume against pore radius of the NiS–ZnS NC; and (f) XRD spectra of the pure NiS, ZnS, and the optimized NiS–ZnS NC.

hexagonal NiS were observed at 2θ values of 34.05°, 34.78°, and 45.62° (JCPDS # 01-077-1624), corresponding to the (002), (101), and (102) planes, respectively (Fig. 2f). The cubic zinc sulfide exhibited prominent peaks at 2θ values of 28.51°, 47.63°, 56.42°, 69.70°, and 77.01°, corresponding to the planes of (111), (220), (311), (400), and (331), respectively, and matched well with JCPDS #00-005-0566.[57] The nanocomposite (NC) exhibited peak positions similar to those for the pure nanoparticles (NPs), with a slight shift toward higher 2θ values observed for the (040) plane of Ni_7S_6 located at $2\theta = 19.44°$ and the (311) plane of ZnS situated at $2\theta = 56.42°$. The crystallite sizes of the pure NiS and ZnS, calculated using Scherrer's equation (eqn (7)), were found to be 23.90 and 4.21 nm, respectively.[32] The shift in peaks indicates a reduced crystallite size (~1.98 nm) for the NiS–ZnS NC, resulting from phase coexistence with smaller lattice parameters.[34,58] The results demonstrate the successful synthesis of the NiS–ZnS NC and highlight its potential for environmental remediation and photocatalytic applications. The observed low crystallinity is attributed to the synthesis conditions, as the material is used without calcination to preserve its surface–active properties for photocatalysis.

Electron images and EDX spectra of the NiS–ZnS NC

Electron images of the NC recorded at multiple positions demonstrate consistent morphology across the material (Fig. S2). The corresponding EDX spectra collected from different regions show nearly identical elemental compositions, indicating a slightly higher weight percentage of nickel compared to zinc throughout the NC, confirmed by EDX analysis (Fig. S2 and Table S1). The high sulfur content further confirms the successful formation of the NiS–ZnS NC. A minor amount of oxygen suggests slight surface oxidation, while the trace sodium observed originates from the Na_2S precipitating agent.

TEM analysis of the NiS–ZnS NC

Transmission electron microscopy (TEM) was employed to examine the morphology and particle-size distribution of the NiS–ZnS NC. TEM images reveal highly agglomerated particles with rough edges and rough surfaces (Fig. 3a and b), consistent with SEM observations (Fig. 2a–c). The average particle size was determined to be approximately 20.8 nm, confirming the nanoscale nature of the synthesized NC (Fig. 3c). The observed agglomeration is attributed to strong interparticle interactions among the nanocomposite components. Such observations provide an in-depth understanding of the particle's morphological and structural features.[58]

TEM analysis of the NiS–ZnS NC showcased well-defined lattice fringes with interplanar spacings of 0.319 nm and 0.285 nm, corresponding to the (111) plane of cubic ZnS and the (002) plane of hexagonal NiS, respectively. These values are in good agreement with the crystallographic data, proving the successful formation of the NiS–ZnS NC (Fig. 3d and e).[59] A slight shift in *d*-spacing is observed, which may be attributed to lattice deformation and strain arising from the interfacial interaction between the NiS and ZnS phases.[34]

Fig. 3f shows the selected area electron diffraction (SAED) pattern, which exhibits distinct diffraction rings, indicating the polycrystalline nature of the NiS–ZnS NC. The diffraction rings can be indexed to the (111), (220), and (311) planes of ZnS, the (002) plane of NiS, and additional reflections (such as (040) and (131)) corresponding to Ni_7S_6. The results are consistent with

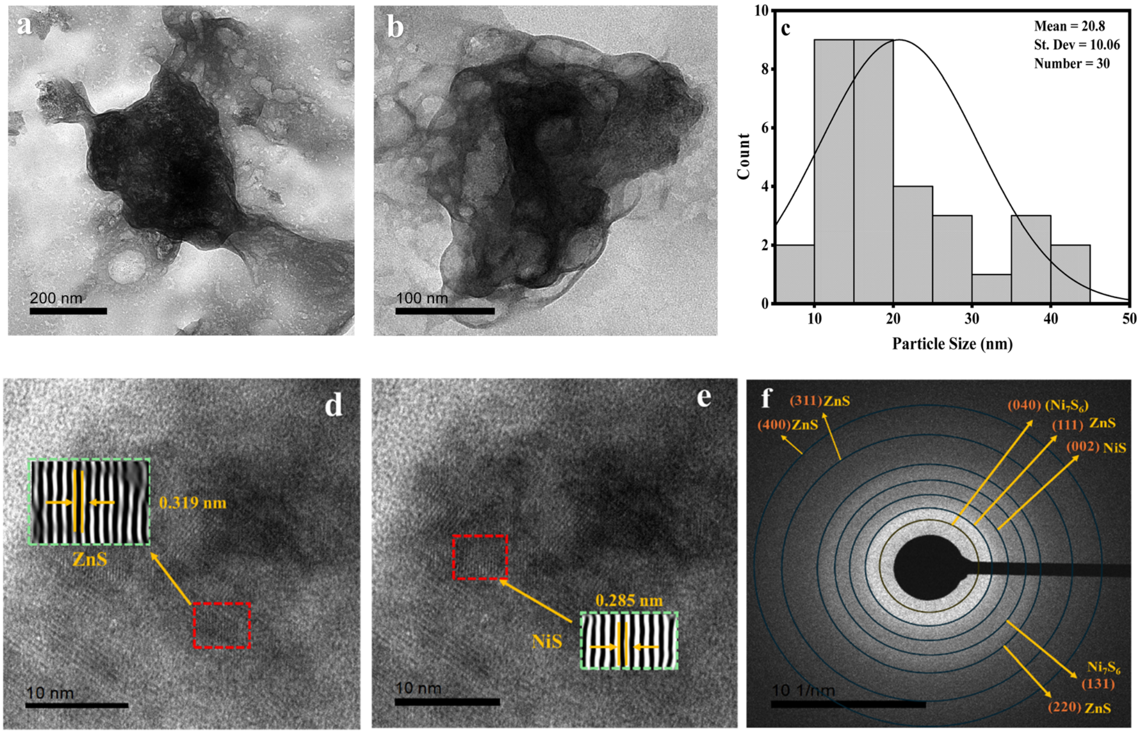

Fig. 3 (a, b, d and e) TEM images, (c) particle-size distribution histogram, and (f) selected-area electron diffraction images of the NiS–ZnS NC.

the XRD analysis and further signify the coexistence of the crystalline NiS and ZnS phases of the nanocomposite.

TGA analysis of the NiS–ZnS NC

The thermal stability of the NiS–ZnS NC was analyzed by TGA over a temperature range of 35 to 800 °C at a heating rate of 10 °C min^{-1}. The TGA curve shows four distinct weight-loss stages, with a total mass loss of 27.2% (Fig. 4). The initial weight loss of 5.9% (35–193.3 °C) is associated with the removal of physically adsorbed and bound water molecules. The second stage, accounting for a 7.87% loss (193.3–303.6 °C), was attributed to the decomposition of residual precursors, surface-bound species, and chemisorbed hydroxyl groups.[60–62] A further weight loss of 6.02% (303.6–475.7 °C) was observed, attributed to the partial loss of sulfur species from the NiS phase at elevated temperatures. Beyond 450 °C, the mass change becomes minimal, indicating the enhanced thermal stability of the nanocomposite.[63] A final weight loss of 2.68% (475.7–712.6 °C) is ascribed to the gradual oxidation of ZnS within the nanocomposite matrix.[64] The residual mass of 72.8%. confirms the overall robustness of the NiS–ZnS NC.

XPS analysis of the NiS–ZnS NC

X-ray photoelectron spectroscopy (XPS) was employed to elucidate the surface composition and bonding environment of the optimized NiS–ZnS NC. The survey spectrum (Fig. 5f) confirms Ni, Zn, and S as the principal elements, with minor contributions from C and O, in good agreement with the EDX results (Fig. S2). The corresponding core-level regions are observed at 850–890 eV for Ni 2p, 1015–1050 eV for Zn 2p, 158–174 eV for S 2p, 280–292 eV for C 1s, and 526–538 eV for O 1s (Fig. 5a–e), indicating that the detected species are chemically bound rather than present as metallic impurities.

In the high-resolution Zn 2p spectrum (Fig. 5b), a sharp doublet appears at 1021.8 and 1044.9 eV, attributable to Zn 2p$_{3/2}$ and Zn 2p$_{1/2}$ of Zn^{2+}, respectively, with a spin–orbit splitting of 32.1 eV, consistent with the reports in the literature.[34] The Ni 2p region (Fig. 5a) displays characteristic peaks at 856.0 eV (Ni 2p$_{3/2}$) and 873.5 eV (Ni 2p$_{1/2}$), together with additional components in the ranges of 852.1–858.4 and 870.8–876.0 eV, which arise from the Ni^{2+} species and their associated satellite features.

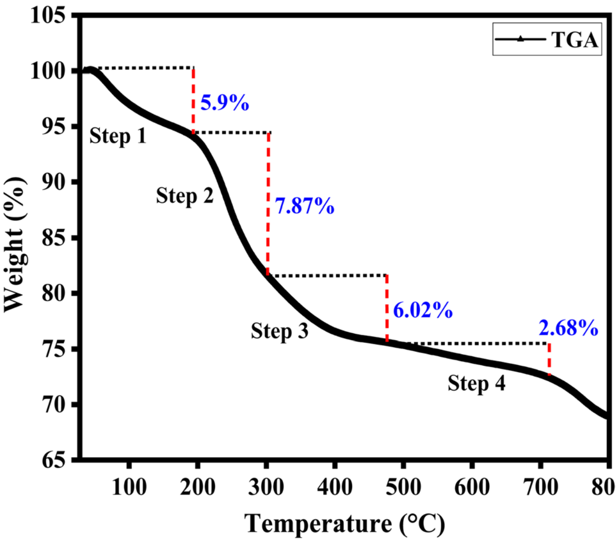

Fig. 4 TGA (weight %) plot of the NiS–ZnS NC.

The spin–orbit separation of 17.5 eV and the presence of shake-up satellites further corroborate the divalent state of Ni in a sulfide environment.

The S 2p spectrum (Fig. 5c) can be deconvoluted into a doublet assigned to S 2p$_{3/2}$ (160.3–163.3 eV) and S 2p$_{1/2}$ (162.5–166.5 eV), characteristic of the lattice S^{2-} in the metal sulfides.[65] This profile confirms that sulfur is predominantly present as sulfide species, associated with both the ZnS and NiS domains, evidencing the formation of an integrated NiS–ZnS network. The C 1s spectrum (Fig. 5d) shows contributions at 284.7, 285.6 and 288.7 eV, which can be ascribed to the C–C/C–H, C–O and O–C═O groups, respectively, while the O 1 s region (Fig. 5e) exhibits a broad peak between 528.6 and 534.9 eV, originating from surface hydroxyls, adsorbed oxygen and minor metal–oxygen bonds.[66] The NiS–ZnS NC exhibits slight shifts in binding energies compared to the pristine NiS and ZnS, as revealed by XPS analysis. Specifically, the Zn $2p_{3/2}$ peak shifts from 1021.8 to 1021.4 eV, while the Ni $2p_{3/2}$ peak shifts from 856 to 855.7 eV. In contrast, a marginally positive shift is observed in the S 2p peak (168.4 to 168.5 eV). These shifts indicate strong electronic interactions between the two sulfide phases (Fig. 5f). The observed negative shift in the Zn and Ni binding energies exhibits interfacial charge redistribution, confirming the formation of a heterostructure and facilitating enhanced charge transfer, which contributes to improving the photocatalytic activity of the nanocomposite.[65] Overall, the XPS data demonstrate that the nanocomposite consists of well-defined Ni^{2+} and Zn^{2+} sulfide phases with clean sulfide bonding environments, confirming the successful synthesis of the NiS–ZnS NC.

Spectroscopic properties

Spectroscopic analyses were performed to confirm the synthesis, electronic structure, and functional properties of the NiS and ZnS nanoparticles (NPs) and the NiS–ZnS NC. UV-Vis absorption spectra (Fig. 6a) verified the successful synthesis of the nanomaterials, with estimated indirect band gaps of 2.62 eV for NiS, 2.48 eV for ZnS, and 2.57 eV for the NC (Fig. 6b).[67] These values indicate that both pure phases and the composite are active under visible light, a prerequisite for efficient photocatalysis.

Photoluminescence (PL) spectra provided further insights into charge carrier dynamics. While ZnS exhibited strong emissions associated with rapid recombination, its intensity was markedly quenched for the NiS–ZnS NC (Fig. 6c), confirming suppressed e$^-$/h$^+$ recombination upon heterojunction formation.[68]

In the NC, photogenerated electrons transfer from the conduction band (CB) of ZnS to that of NiS, where they participate in oxygen reduction to generate reactive oxygen species (ROS and $^{\bullet}O_2^{-}$). Simultaneously, holes produced in the valence band (VB) of NiS migrate to the VB of ZnS, enabling the

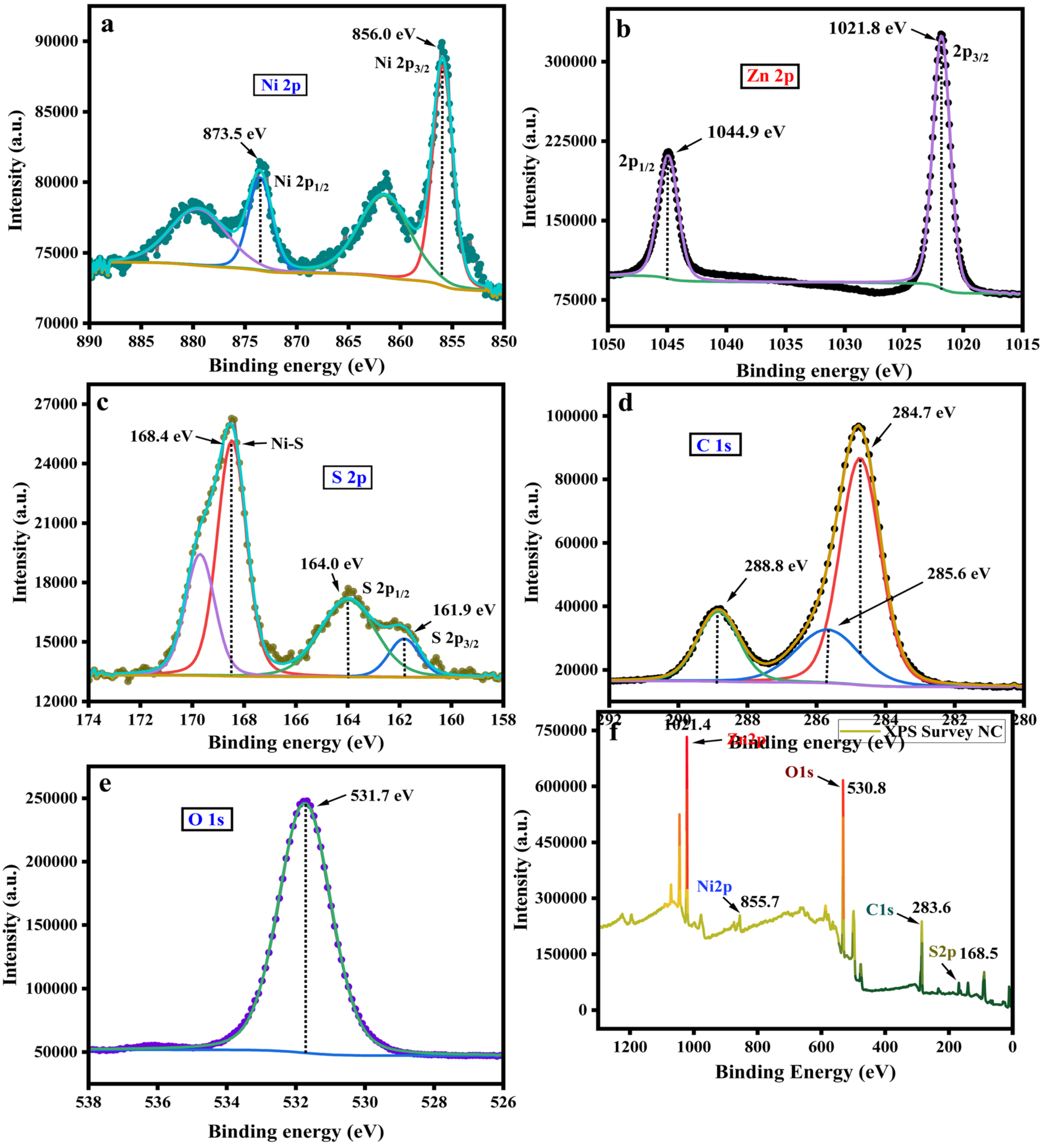

Fig. 5 (a) High-resolution XPS spectra of nickel (Ni), (b) zinc (Zn), (c) sulfur (S), (d) carbon (C), and (e) oxygen (O) and the (f) typical XPS survey spectrum of the NiS–ZnS NC.

oxidation of hydroxyl ions to hydroxyl radicals ($^{\bullet}$OH). These ROS act as highly reactive species responsible for the degradation of crystal violet.

Notably, the higher PL intensity observed for pure NiS is consistent with the defect-related or exciton-mediated transitions commonly reported for NiS nanoparticles.[69,70] Together, these results demonstrate that the ZnS–NiS heterojunction enhances charge separation, prolongs carrier lifetimes, and promotes radical generation, thereby underpinning the superior photocatalytic performance of the NC. Table 1 below shows the band gap analysis from the PL spectra, which mostly prioritizes the visible light–active region in all nanomaterials.

Fourier-transform infrared (FTIR) spectra were recorded in the 500–600 cm^{-1} range to examine the characteristic stretching and bending vibrations of the nanomaterials (Fig. 6d). For the pure NiS and ZnS, distinct bands were observed at 514, 529, 505, 518, and 524 cm^{-1}, corresponding to the Ni–S and Zn–S vibrations. For the NiS–ZnS NC, these bands shifted to 503, 509, and 526 cm^{-1}, indicating interfacial interactions between NiS and ZnS and the possible emergence of new vibrational modes associated with nanocomposite formation. Such band shifts provide strong evidence for the successful integration of the two phases.

The full FTIR spectra (Fig. S3) further confirmed the structural features. For NiS, absorptions between 514–529 cm^{-1} and

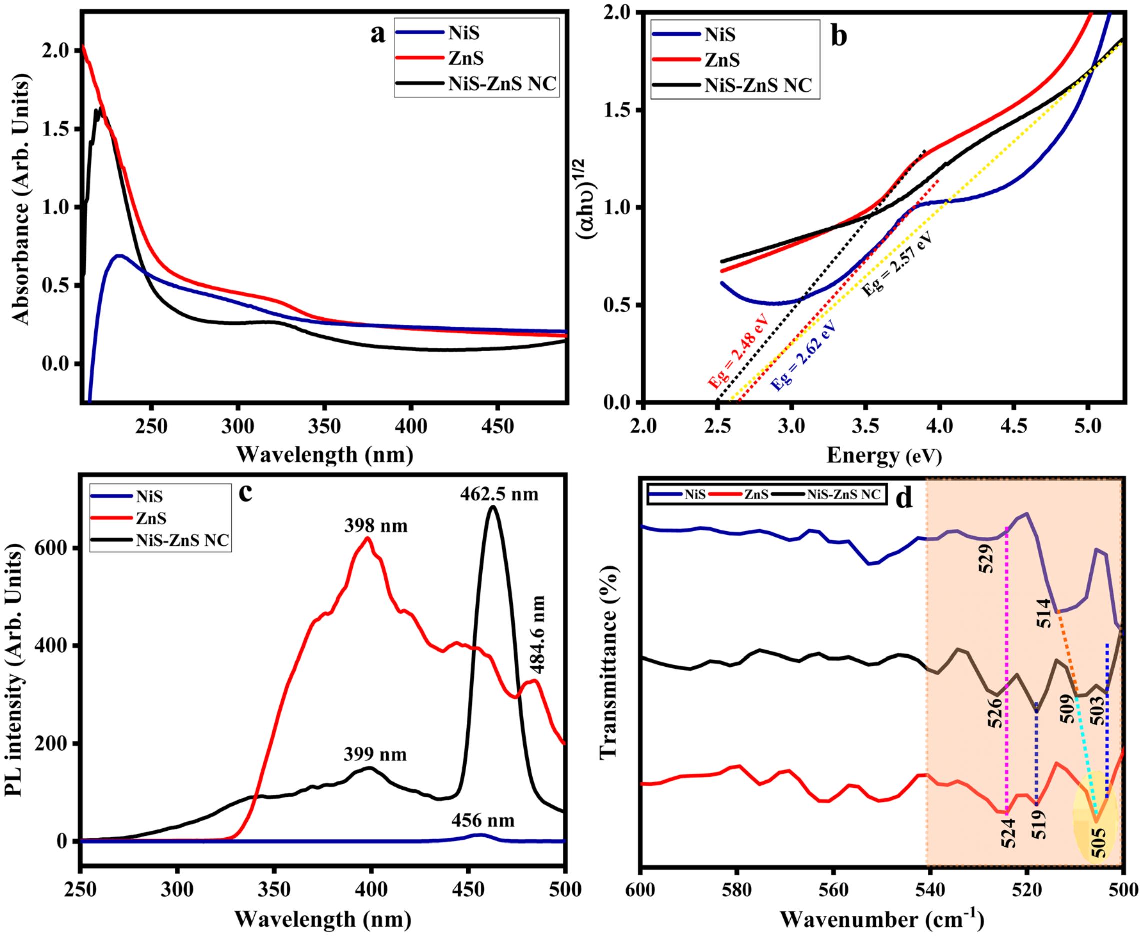

Fig. 6 (a) UV-vis spectra (0.1 mg mL^{-1}, T: 20 °C); (b) indirect band gap calculated from Tauc plot; (c) fluorescence spectra (0.1 mg mL^{-1}, T: 20 °C); and (d) FTIR spectra of NiS, ZnS, and the NiS–ZnS NC.

Table 1 Excitation and emission wavelengths of pure NiS and ZnS NPs and the NiS–ZnS NC

Excitation wavelength (nm)	Emission wavelength (nm)	Band gap (eV)
NiS (226)	456	2.72
ZnS (306)	398	3.11 & 2.56
NiS–ZnS (231 & 306)	399 & 462.5	3.10 & 2.68

at 1548 cm^{-1} are attributed to the Ni–S asymmetrical stretching and adsorbed water, respectively.[71] Additional bands at 1011–1089 cm^{-1} suggest Ni–S–Ni bending modes.[72] In ZnS, peaks at 1401 and 1548 cm^{-1} correspond to the symmetric and asymmetric stretching of zinc carboxylate (COO^{-}), while a broad band at 3221 cm^{-1} arises from the O–H stretching of surface-adsorbed water. A weaker peak near 1116 cm^{-1} can be assigned to S–O stretching vibrations.[73]

Overall, FTIR analysis validates the presence of Ni–S and Zn–S bonds, confirms nanocomposite formation through vibrational shifts, and highlights the surface functionalities relevant to the dye interaction and photocatalytic activity.

Screening studies

The NiS–ZnS NC demonstrated excellent photocatalytic activity against cationic dyes, achieving degradation efficiencies of 98% for crystal violet (CV), 95% for malachite green (MG), and 94% for methylene blue (MB) (Fig. 7a). In contrast, the NC exhibited only limited activity toward anionic dyes, highlighting its preferential affinity for cationic species. These results confirm that the NiS–ZnS heterojunction is optimally designed for targeting positively charged dye molecules, where surface charge interactions play a critical role. Among the cationic dyes, CV was chosen as the model pollutant for detailed optimization and mechanistic investigation, providing insights into charge transfer, radical generation, and surface interactions. Findings from CV degradation can thus be extended to other cationic dyes with similar structural and electronic characteristics (Fig. 7a).

Surface-charge control of NC

Zeta potential measurements confirmed the negatively charged nature of the NiS–ZnS NC, with a value of −14.7 ± 0.9 mV under neutral conditions and a point of zero charge (PZC) at pH 2.67 (Fig. 7b). Below the PZC, the NC surface becomes positively

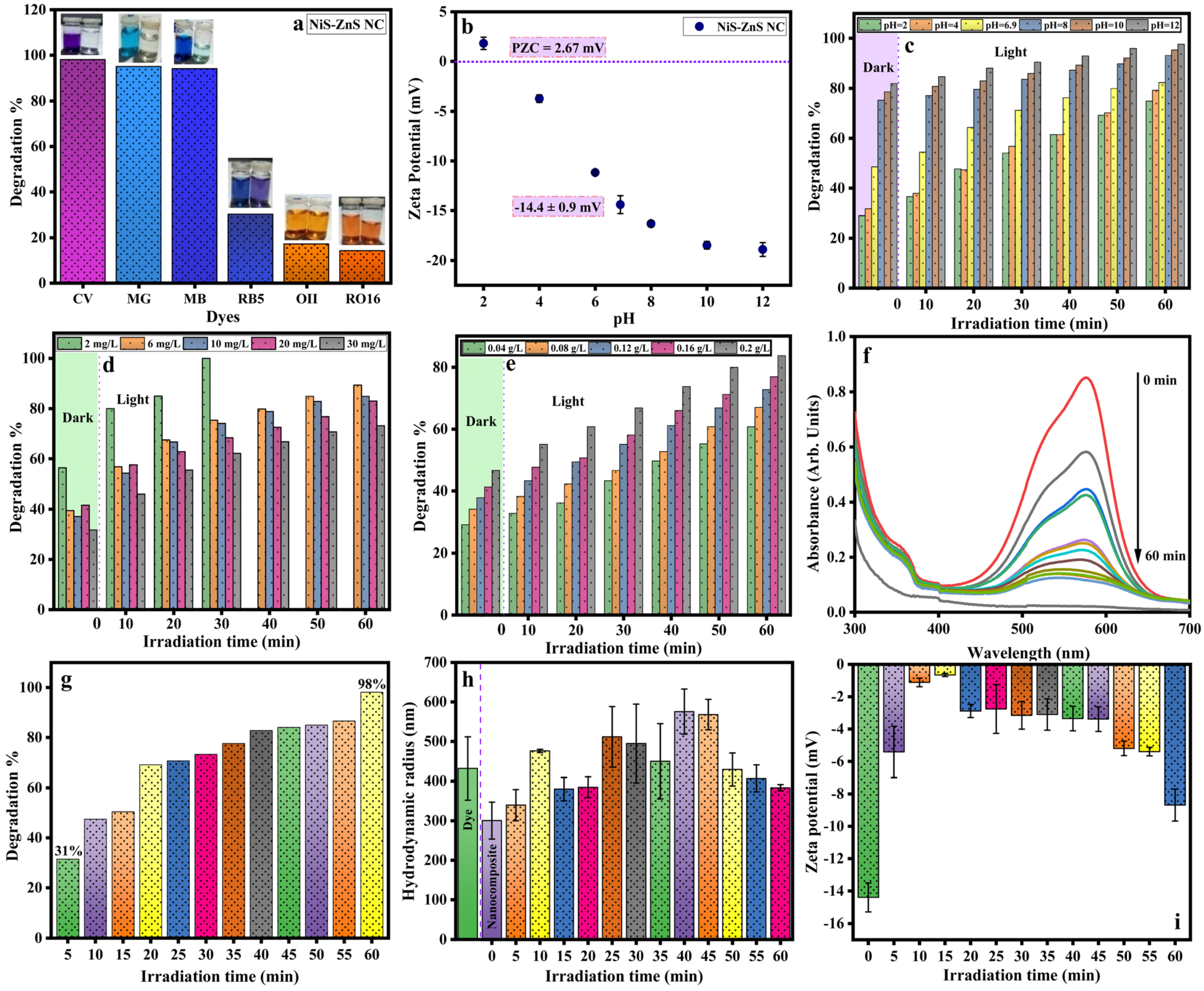

Fig. 7 (a) Screening studies (dye concentration: 50 mg L^{-1}, dose: 1 g L^{-1}, irradiation time: 60 min); (b) ζ potential of NC at various pH (concentration: 0.2 g L^{-1}, sonication duration: 30 min); (c) effect of pH (CV concentration: 20 mg L^{-1}, dose: 0.2 g L^{-1}, T: 20 °C); (d) effect of concentration (dose: 0.2 g L^{-1}, T: 20 °C, pH: 6.9); (e) effect of dose (CV concentration: 20 mg L^{-1}, T: 20 °C, pH: 6.9); (f) UV-vis spectra of CV dye before and after degradation; (g) percent degradation profile, (h) H_R size, and (i) ζ potential of NC during dye degradation (dose: 0.4 g L^{-1}, CV concentration: 20 mg L^{-1}, pH: 6.9).

charged. In contrast, above it, the charge is increasingly negative, reaching −18.9 ± 0.7 mV at a high pH of 12. The progressive increase in the negative potential is attributed to the enrichment of surface –OH groups.[74] Such charge behavior is highly favorable for dye adsorption. Crystal violet (CV), a cationic dye, exhibits a positive surface potential of +1.41 mV at pH 6.9, enabling strong electrostatic attraction towards the negatively charged NC. These interactions significantly promote dye adsorption, which serves as a key prerequisite for subsequent photocatalytic degradation.

Effect of different parameters on CV degradation

The influence of various parameters on CV photocatalytic degradation has been investigated, including solution pH, initial CV concentration, and photocatalyst dose using the NiS–ZnS NC.

Cationic dye photocatalytic degradation by NC

Effect of solution pH. The solution pH strongly influenced the dye adsorption and photocatalytic degradation, primarily due to electrostatic interactions between the negatively charged NiS–ZnS NC surface and the positively charged crystal violet (CV) dye. As shown in Fig. 7c, dye adsorption increased from 28.9% at pH 2 to 74.9% at pH 12, consistent with the increasing negative surface potential of the NC at higher pH values (Fig. 7b). The photocatalytic degradation efficiency exhibited a similar trend, rising from 78.6% to 95.3% as pH increased from 2 to 12. The corresponding degradation rate constants increased with pH (Fig. S7a), confirming that stronger electrostatic attraction facilitates dye adsorption and accelerates radical-mediated degradation.

Effect of the initial dye concentration. The photocatalytic efficiency of NC decreased with increasing CV concentration

(Fig. 7d). At 2 mg L^{-1}, complete degradation was achieved within 30 min, whereas efficiency dropped to 88.3%, 86.2%, 81.6%, and 73.2% at 6, 10, 20, and 30 mg L^{-1}, respectively. This inverse relationship between the dye concentration and the degradation efficiency is consistent with previous reports.[75] The decline arises from the limited availability of active sites at higher dye loadings and reduced light penetration through concentrated dye solutions, which collectively suppress radical generation.[76] Kinetic analysis using the pseudo-first order (PFO) model further supported this observation, with rate constants (k) decreasing from 0.026 min^{-1} at 2 mg L^{-1} to 0.012 min^{-1} at 30 mg L^{-1} (Fig. S7b).

Effect of photocatalyst dose. Catalyst loading is a critical factor in balancing photon absorption with material economy. As shown in Fig. 7e, increasing the NC dose from 0.04 to 0.2 g L^{-1} improved the degradation efficiency from 67.9% to 83.7%. This enhancement is attributed to the greater number of active sites available at higher dosages.[77] Importantly, NC maintained strong photocatalytic performance even at low doses, underscoring its efficiency. Kinetic analysis confirmed this trend, with the PFO rate constant rising from 0.008 min^{-1} at 0.04 g L^{-1} to 0.015 min^{-1} at 0.2 g L^{-1} (Fig. S7c).

Mineralization efficiency. Total organic carbon (TOC) analysis was performed to confirm CV mineralization and rule out accumulation of harmful intermediates. For a 20 mg L^{-1} dye solution, the initial TOC concentration of 5.08 mg L^{-1} decreased to 1.26 mg L^{-1} after photocatalysis, corresponding to 75.1% TOC removal, alongside 83.4% dye degradation (Fig. S8). This high degree of TOC elimination indicates that CV was oxidized predominantly to CO_2 and H_2O, rather than transformed into persistent organic by-products, as confirmed by LC-MS analysis (Fig. 13a).

Mechanistic and DLS confirmation of CV degradation

A new strategy was employed to investigate the dynamic interaction between dye molecules and the photocatalyst during degradation by monitoring the H_R and surface charge (ζ potential) of the NiS–ZnS NC in real time. Dynamic light scattering (DLS) provides valuable information on particle-size distribution and colloidal stability in terms of surface charge, and tracking these parameters under photocatalytic conditions reveals the interplay between dye adsorption and degradation at the catalyst surface.

UV-visible and degradation profiles

The photocatalytic reaction shows that the NC rapidly initiated the degradation of crystal violet (CV) (Fig. 7f and g). Approximately 31% of the dye was removed within the first five min of irradiation, and complete degradation (98%) was achieved by 60 min (Fig. 7g). The disappearance of the major absorption band at 576 nm further confirmed the breakdown of the dye structure (Fig. 7f).

Hydrodynamic radius (H_R) variation

The H_R of the NC changed dynamically throughout the degradation process (Fig. 7h). In the first 10 min, H_R increased, indicating the adsorption of dye molecules onto the NC surface, supported by surface-charge variation (Fig. 7i). Between 10 and 20 min, H_R decreased, consistent with the photocatalytic breakdown of the adsorbed dye. Beyond 20 min, H_R fluctuations with larger standard deviations suggested alternating phases of adsorption and partial degradation, likely due to the transient accumulation of dye and intermediates. After 40 min, a continuous decline in H_R was observed, reflecting sustained degradation and progressive removal of dye molecules in the final stage of the cycle. This systematic H_R variation provides direct evidence of adsorption-degradation coupling at the NC surface.

Zeta potential evolution

Surface-charge monitoring further confirmed the electrostatic interactions driving adsorption and degradation. Initially, the NC exhibited a ζ potential of −14.4 ± 0.9 mV. Within 5 min of contact with CV, this value shifted to −5.4 ± 1.6 mV and to −0.66 ± 0.09 mV by 10 min, consistent with the strong adsorption of positively charged (+1.41 mV) dye molecules (Fig. 7i). As degradation progressed, the ζ potential gradually recovered to −8.7 ± 0.9 mV by the end of the reaction, indicating the removal of adsorbed dye and partial desorption of mineralized products. The partial loss of the negative charge is attributed to the deposition of oxidized intermediates and residual mineralization products on the NC surface. Together, H_R and ζ potential measurements provide complementary evidence for the dynamic adsorption-degradation mechanism.

Kinetic performance

The effect of the initial CV concentration (2–30 mg L^{-1}) on the adsorption capacity (q_t, mg g^{-1}) was evaluated, with equilibrium attained within 20 min (Fig. S6). The q_t increased from 7.3 to 47.15 mg g^{-1}, with increasing CV concentration, which can be attributed to enhanced interaction between dye molecules and the available active sites on the nanocomposite surface.[78] To further evaluate the photocatalytic activity, the degradation of CV was examined at initial concentrations ranging from 2 to 30 mg L^{-1} (Fig. 8a). The results show a clear decrease in degradation efficiency with increasing dye concentration, attributable to the saturation of active sites and reduced light penetration at higher loadings. Complete degradation occurred within 30 min at 2 mg L^{-1}, while efficiency dropped to 88.3%, 86.2%, 81.6%, and 73.2% at 6, 10, 20, and 30 mg L^{-1}, respectively. Pseudo-first-order kinetic analysis revealed a decrease in the rate constant (k) from 0.026 min^{-1} at 2 mg L^{-1} to 0.012 min^{-1} at 30 mg L^{-1}, in agreement with literature trends.

At low initial CV concentrations, the NiS–ZnS NC achieved complete degradation within 30 min. In contrast, efficiency decreased to 73% at a higher concentration of 30 mg L^{-1} (Fig. 8a). Control experiments, in which the CV solution was irradiated in the absence of NC, displayed only 8.9% degradation, confirming that the process is predominantly photocatalyst-driven. The decline in the degradation efficiency at higher concentrations is attributed to the saturation of active sites on the NC surface and the reduced light penetration in

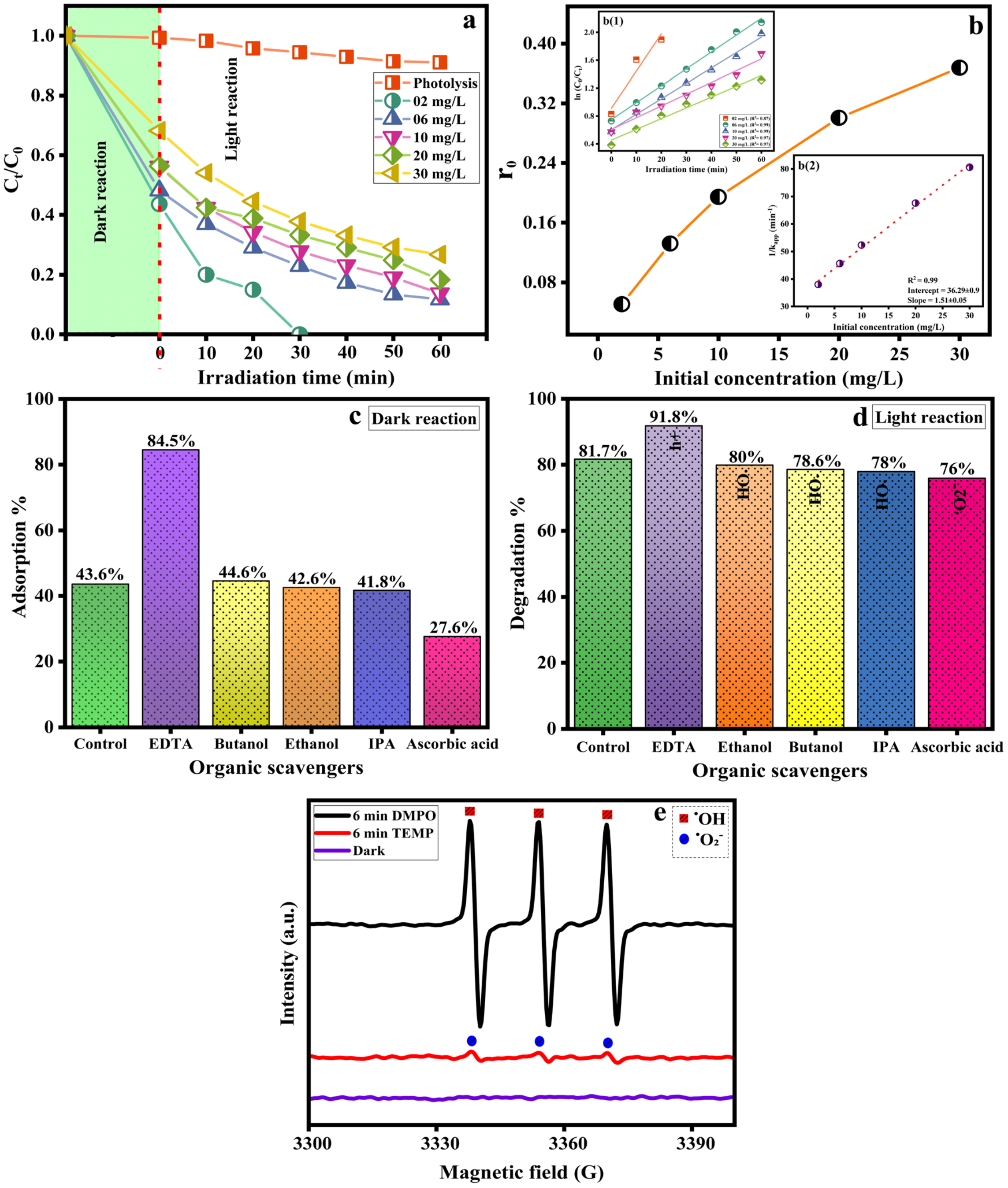

Fig. 8 (a) Photocatalyst performance. (b) Photocatalytic kinetics (reaction rate *vs.* initial CV conc.): (b_1) PFO kinetic curve (inset) and (b_2) plot of $1/K_{app}$ *vs.* initial CV conc. (inset) (dose: 0.2 g L^{-1}, pH: 6.9, T: 20 °C). (c) Effect of organic scavengers on adsorption. (d) Photocatalytic degradation (10 mL (0.1 M) in a 50 mL solution, dose: 0.2 g L^{-1}, CV concentration: 20 mg L^{-1}, pH: 6.9, T: 20 °C). (e) EPR spectra of $^{\bullet}OH$ and $O_2^{\bullet-}$ when DMPO and TEMP were used as trapping agents under dark and light conditions, respectively (DMPO and TEMP concentrations: 20 mg L^{-1}, T: 20 °C, pH: 6.9, dose: 0.2 g L^{-1}, light source: 500 W halogen lamp).

concentrated dye solutions, both of which suppress radical generation and retard the overall reaction.[43]

The photocatalytic data were fitted to a pseudo-first-order kinetic model, $\ln(C_0/C_t) = k_1t$, which showed an excellent correlation with the experimental results (R^2 values), as shown in Fig. 8(b_1).[79] The apparent rate constant (k_{app}) decreased systematically with increasing dye concentration, reflecting reduced reaction rates at higher pollutant loads. Such rapid removal at lower concentrations is consistent with greater availability of active sites and higher surface-to-volume ratios for dye-catalyst interactions.[80]

To further describe the heterogeneous photocatalytic process, the Langmuir–Hinshelwood (L–H) model was applied. The inset (Fig. 8b_2) shows a linear relationship between $1/k_{app}$ and the initial CV concentration, confirming the L–H mechanism. From this plot, the surface reaction rate constant (K_C) was calculated as 0.69 mg L^{-1} min^{-1} (from the slope, $1/K_C$; $R^2 = 0.99$), while the adsorption equilibrium constant (K_{L-H}) was determined to be 0.042 L mg^{-1} (from the intercept, $1/K_CK_{L-H}$).[81] The relatively high K_C value indicates that the degradation process is primarily driven by photocatalytic reactions rather than adsorption alone.[82]

These results highlight that while NC efficiently degrades CV across a wide concentration range, its performance is strongly influenced by the initial pollutant load, with its kinetic behavior well described by the L–H model.

Tuning NC activity using organic scavengers

To investigate the reactive species involved in the photocatalytic process, scavenger experiments were performed (Fig. 8c). The addition of isopropanol (IPA) and ethanol, well-established $^{\bullet}OH$ scavengers, resulted in a slight decrease in both the dye adsorption and photocatalytic efficiency, confirming the involvement of $^{\bullet}OH$ radicals. This observation is consistent with previous reports showing that short-chain alcohols effectively quench $^{\bullet}OH$ radicals and suppress photocatalytic degradation pathways.[83] Additionally, both ethanol and IPA can act as hole scavengers, reducing hole-driven oxidation and thereby decreasing degradation efficiency.[84]

In contrast, butanol exhibited a slight increase in adsorption (43.6% to 44.6%) but a marginal reduction in degradation efficiency. This behavior is attributed to the weaker radical scavenging of long-chain alcohols, as well as the steric and polarity effects that influence their interaction with the radical surface.[85]

The presence of EDTA significantly enhanced performance, with degradation efficiency reaching 91.8%. This improvement arises from its dual role: (i) increasing dye adsorption (43.6% to 84.5%) by enhancing surface charge and electrostatic attraction with cationic CV[86] and (ii) acting as a hole scavenger, thereby suppressing the e^-/h^+ recombination and promoting reactive oxygen species generation.[87] The nearly colorless solution observed under dark conditions further confirms the strong adsorption capability induced by EDTA.[88]

Ascorbic acid, used as a superoxide radical ($^{\bullet}O_2^-$) scavenger, led to a significant decrease in both adsorption and degradation, suggesting a notable contribution of $^{\bullet}O_2^-$ radicals to the photocatalytic process (Fig. 8d).[89]

Overall, the degradation efficiency followed the order: EDTA > NC (no scavenger) > ethanol > butanol > IPA > ascorbic acid, indicating that although scavengers influence performance, the NC retains a high activity, reflecting its robust charge separation and transfer characteristics.

Further evidence from EPR analysis supports the involvement of reactive oxygen species (Fig. 8e). The lack of an EPR signal under dark conditions confirms that ROS generation by the nanocomposite is strictly light-induced and monitored through spin trapping using DMPO and TEMP.[90] The oxidation of 5,5-dimethyl-1-pyrroline *N*-oxide (DMPO) to its corresponding radical species verifies the presence of $^{\bullet}OH$ radicals, while the inhibition of CV degradation in the presence of ascorbic acid confirms the involvement of $^{\bullet}O_2^-$ radicals. Additionally, the conversion of 2,2,6,6-tetramethylpiperidine (TEMP) into 2,2,6,6-tetramethylpiperidine-1-oxyl (TEMPO) indicates the generation of singlet oxygen species. These results collectively confirm that multiple reactive oxygen species contribute to the photocatalytic degradation mechanism.[91]

Computational study of NiS, ZnS, and the NiS–ZnS NC

Density functional theory (DFT) calculations were performed using the B3LYP functional with the STO-3G basis set to gain molecular-level insight into the electronic properties of the NiS–ZnS nanocomposite (NC). The geometries of individual NiS and ZnS nanostructures were first optimized, both adopting cage-like configurations that maximize surface area and provide abundant active sites. Subsequently, the composite NiS–ZnS structure was modeled and further combined with crystal violet (CV) to evaluate dye-catalyst interactions.

Frontier molecular orbital (HOMO–LUMO) analysis was carried out to probe electronic distributions and band gap energies (Fig. 9a). In the orbital maps, deep red regions denote high electron density, while green regions indicate low density. Compared to pristine NiS and ZnS, the NiS–ZnS NC exhibited a significant reduction in band gap energy (Table S3), reflecting enhanced charge delocalization and improved electron–transfer pathways within the heterojunction. This band gap narrowing underscores the nanocomposite's capacity to absorb visible light more efficiently than its individual components.

The HOMO–LUMO orbital distributions of NiS, ZnS, NiS–ZnS, and CV (Fig. 10) further illustrate favorable orbital overlap between the dye and NC, suggesting efficient electron injection from the excited dye into the composite conduction band. These computational results corroborate the experimental findings, demonstrating that electronic coupling and band gap reduction in the NiS–ZnS system are key contributors to its superior photocatalytic activity.

Electrostatic potential (ESP) maps were generated to visualize charge distribution within the NiS–ZnS NC and crystal violet (CV), providing molecular-level insight into potential reactive sites (Fig. 9a). These maps highlight electron-rich (nucleophilic) and electron-deficient (electrophilic) regions, thereby identifying preferential sites for intermolecular interactions and photocatalytic reactions.[92] A continuous color gradient from blue to red was used to represent ESP values, with blue denoting regions of high positive potential (electrophilic sites) and red indicating low negative potential (nucleophilic sites).

For CV, the negative potential was predominantly localized near the nitrogen atoms and at the central triphenylmethane core, consistent with known sites of electrophilic attack (Fig. 9a). By contrast, positively charged ESP regions provide favorable docking points for electron-rich species.

The spatial distribution of these potentials suggests that CV molecules align on the NC surface in orientations that maximize electrostatic complementarity, facilitating adsorption and subsequent charge transfer.

Contour plots further confirmed this orientation, showing preferential binding directionality of CV to the nanomaterial surface (Fig. 9a).

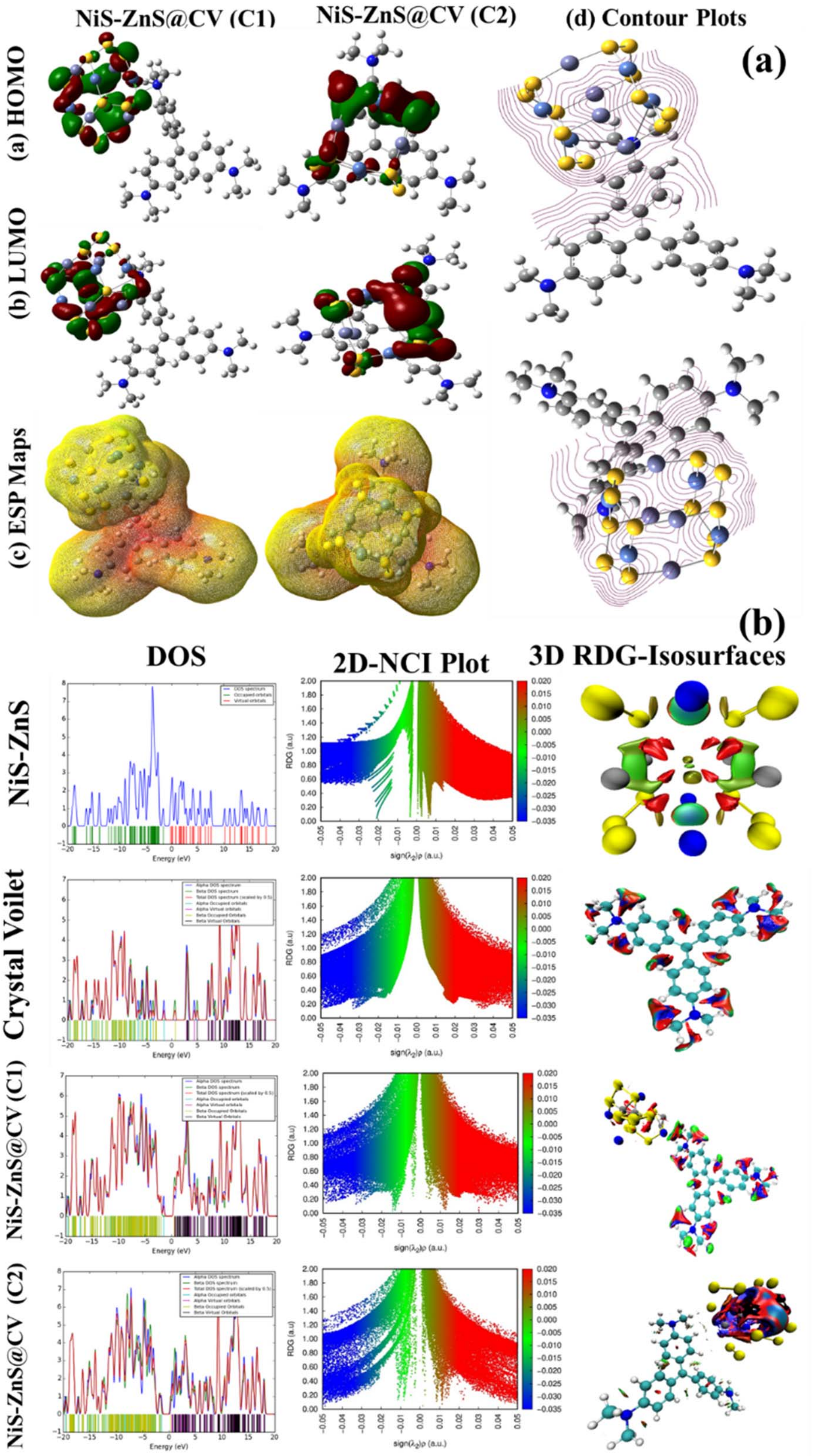

Fig. 9 (a) Optimized structures showing the HOMO, LUMO, ESP maps, and contour plots of the molecular complex systems. (b) DOS, 2D NCI plot, and 3D-isosurfaces of the nanocomposite, dye, and their complexes.

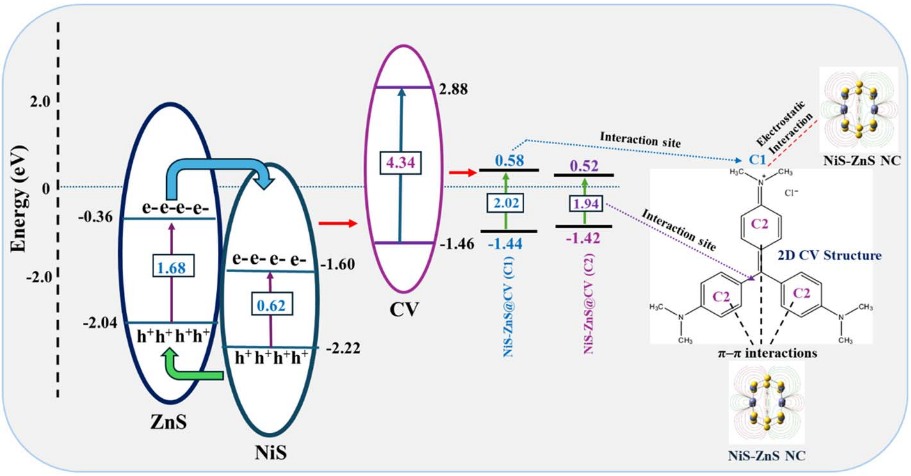

Fig. 10 Charge-transfer mechanism for the NiS–ZnS NC, and its binding mechanism with the C1 and C2 (electron-dense parts) of the CV dye: a theoretical approach.

Overall, ESP mapping complements the HOMO–LUMO analysis, revealing that charge distribution and electrostatic complementarity play decisive roles in stabilizing dye-catalyst interactions and driving efficient photocatalytic degradation.[93]

As summarized in Table S4, the interaction energy of the NiS–ZnS NC with CV (-199.18 kcal mol^{-1}) exceeds values reported for comparable materials, underscoring its superior binding affinity and highlighting its strong potential for efficient visible light–driven photocatalysis. The interaction energies of all stable complexes were calculated according to eqn (8).[94]

$$\Delta E_{\text{int}} = E_{\text{CV@NiS–ZnS}} - (E_{\text{NiS–ZnS}} + E_{\text{CV}}) \tag{8}$$

where ΔE_{int} represents the interaction energy after binding, $E_{\text{CV@NiS–ZnS}}$ represents the total energy of the combined system, $E_{\text{NiS-ZnS}}$ represents the energy of the photocatalyst, and E_{CV} represents the energy of the isolated dye molecule.

DOS and NCI-RDG analyses

Density of states (DOS) analysis was carried out to probe the electronic structure of the NiS–ZnS NC and its interaction with crystal violet (CV). DOS provides critical insights into electron–transfer processes between the valence and conduction bands, which directly influence photocatalytic efficiency. The Fermi level, positioned between the valence band maximum and the conduction band minimum, dictates the migration of photoexcited electrons under irradiation.[95]

Upon interaction with CV, the DOS profiles of the NC displayed significant modifications, particularly in the energy distribution near the conduction band. Pronounced changes were observed in the lowest unoccupied molecular orbital (LUMO) region, accompanied by shifts in the overall density distribution. These features reflect the enhanced electronic coupling between the dye and nanocomposite, which effectively lowers the charge-transfer barrier.

Such electronic reorganization indicates that the adsorption of CV facilitates stronger orbital overlap and promotes efficient migration of electrons from the dye to the NC. This improved charge-transport pathway not only enhances the separation of photogenerated carriers but also increases the likelihood of radical formation at the catalyst surface. Collectively, the DOS results corroborate experimental observations and highlight the role of dye-nanocomposite interactions in driving superior photocatalytic activity.[95]

Frontier orbital calculations revealed clear electronic modifications upon dye adsorption. The LUMO energy of the pristine NiS–ZnS NC was -0.17 eV, while that of crystal violet (CV) was 2.88 eV. Upon interaction, the LUMO levels of the combined systems shifted markedly to 0.58 eV at the C1 site and 0.52 eV at the C2 site. This downward shift enhanced the electronic coupling between the dye and the NC, facilitating efficient electron transfer across the interface. The interaction-induced changes in the frontier orbitals reflect the formation of a favorable dye–nanocomposite junction, which promotes the separation of photoinduced e^-/h^+ pairs under irradiation. These results are consistent with the calculated interaction energies and experimental photocatalytic performance, further validating the superior activity of NiS–ZnS in the presence of CV.

To gain deeper insights into the binding forces at the interface, non-covalent interaction (NCI) analysis was performed. Based on the electron density (ρ) and the reduced density gradient (RDG), this method distinguishes attractive forces [$\text{sign}(\lambda_2)\ \rho < 0$], steric repulsion [$\text{sign}(\lambda_2)\ \rho > 0$], and weak dispersive interactions [$\text{sign}(\lambda_2)\ \rho \approx 0$].[96] The 2D NCI plots (Fig. 9b) revealed distinct green and blue spikes within the $\text{sign}(\lambda_2)\rho$ range of 0 to -0.05 a.u., confirming the coexistence of van der Waals and electrostatic interactions. Strong blue spikes (-0.02 to -0.05 a.u.) correspond to attractive forces localized near the aromatic rings and nitrogen functionalities of CV, in agreement with the reduced band gaps (from 4.34 to 2.02/1.94 eV) and high interaction energies (-197.27 and -199.18 kcal mol^{-1}). Green spikes further indicated the contribution of dispersive van der Waals interactions.

Together, these findings demonstrate that CV adsorption on NiS–ZnS is stabilized by multiple non-covalent forces, enabling robust dye-catalyst binding, enhanced charge transfer, and improved photocatalytic efficiency.

Interaction analysis and photocatalytic potential of the NiS–ZnS NC with crystal violet dye

To further elucidate the photocatalytic behavior of the NiS–ZnS nanocomposite (NC), interaction studies were performed with crystal violet (CV) using the optimized geometries of both the NC and dye molecule. Two representative adsorption configurations were examined: (i) the C1 site, corresponding to the branched nitrogen atom of CV, and (ii) the C2 site, located on the aromatic benzene ring, as shown in Fig. 10.

At the C1 site, a strong interaction between NiS–ZnS and CV was observed, leading to a pronounced narrowing of the band gap from 4.34 eV to 2.02 eV and an interaction energy of -197.27 kcal mol^{-1}. The reduced band gap implies enhanced absorption in the visible region, while the large negative interaction energy indicates robust binding at the dye-nanocomposite interface. These effects collectively promote efficient e^{-}/h^{+} separation and facilitate charge transfer, consistent with the high photocatalytic potential of the NC at this site (Fig. 10).

The C2 site exhibited even stronger binding. Here, the band gap decreased to 1.94 eV, accompanied by a more favorable interaction energy of -199.18 kcal mol^{-1}. This enhanced stability is attributed to the strong π-d orbital overlap between the benzene ring of CV and the NC surface, supported by electrostatic contributions that improve electronic communication at the interface. The resulting increase in charge mobility suggests that adsorption at the C2 site may be particularly favorable for driving photocatalytic reactions.

Effect of salts on the surface charge, adsorption, and photocatalytic degradation of CV

This study introduces a novel approach to track surface interactions in photocatalytic systems by simultaneously monitoring the H_R and ζ potential of the NiS–ZnS NC during dye adsorption and degradation. While earlier reports have discussed tuning the surface charge of nanomaterials to control dye interactions, the combined use of H_R and ζ potential[38] to directly validate dye/NC/salt interactions and their role in photocatalysis has not been reported. Here, monovalent and divalent salts with different anions (NaCl, $NaNO_3$, Na_2SO_4, $AgNO_3$, and $CaCl_2$) were employed to modulate the NC surface charge and probe their influence on crystal violet (CV) adsorption and photocatalytic degradation.

Salt–nanocomposite interactions

Pristine NC exhibited an H_R of 300 ± 46.7 nm and a ζ potential of -14.3 ± 1.0 mV in suspension. Upon exposure to 0.1 M salt solutions, H_R generally increased. At the same time, ζ potential shifted toward more positive values, confirming cation binding at the NC surface (Fig. 9a and b), and the values are mentioned in Table S5. Among sodium salts, $NaNO_3$ produced the largest H_R increase and a slight reduction in surface charge, indicating strong NO_3^{-}-mediated interactions. By contrast, NaCl and Na_2SO_4 induced only modest changes, consistent with their limited Cl^{-} and SO_4^{2-} bindings, respectively. $CaCl_2$ induced the greatest reduction in the ζ potential, reflecting a strong adsorption of divalent Ca^{2+} ions at high charge density. $AgNO_3$ had negligible effects, suggesting weak Ag^{+} affinity for sulfide sites; the slight surface charge shift was attributed to the deposition of nitrate ions.

Effect on adsorption

Upon addition, H_R increased with larger deviations, confirming the deposition of CV molecules at the NC surface (Fig. 9a). Simultaneously, the ζ potential shifted toward less negative values (Fig. 9b), validating the electrostatic attraction between the cationic CV and the negatively charged NC. The strongest ζ-potential reduction occurred in the $CaCl_2$ solution due to Ca^{2+} deposition, which reduced the electrostatic binding of CV. In contrast, $NaNO_3$ maintained surface stability after CV adsorption, highlighting the stabilizing role of nitrate ions, as shown in (Fig. 9c).

Effect on photocatalytic degradation

Following irradiation, H_R decreased across all systems, confirming dye breakdown. However, H_R remained slightly higher than in pristine NC, indicating the partial deposition of mineralization products and residual salts. The ζ potential partially recovered toward more negative values, consistent with CV degradation, but it did not return to the initial levels, suggesting that dye fragments and salt ions remained on the surface (Fig. 9b).

Influence of salt on the adsorption and photocatalytic degradation of CV

Adsorption studies after 20 min in the dark further clarified the salt effects (Fig. 11c). $NaNO_3$ produced the highest CV removal efficiency (68.4%), consistent with its strong impact on H_R and ζ potential, where competitive binding between nitrate ions and dye molecules enhanced surface interactions. In contrast, $CaCl_2$ reduced adsorption to 36.7%, as the strong Ca^{2+} binding suppressed electrostatic attraction to CV. Na_2SO_4 slightly enhanced adsorption by promoting diffuse-layer formation, whereas NaCl decreased CV adsorption due to competing dye–salt interactions and reduced NC surface charge. $AgNO_3$ reduced adsorption efficiency despite increases in H_R, attributed to the disruptive role of the large-radius Ag^{+} ions at the dye-NC interface.

Collectively, these results confirm that H_R and ζ potential monitoring provide a powerful means to visualize NC-salt-dye interactions in real time. The data reveal that the salt type and ionic properties strongly modulate the surface charge, adsorption dynamics, and degradation efficiency, thereby shaping photocatalytic performance.

Fig. 11d shows the CV dye photocatalytic degradation by the NiS–ZnS NC in different salts. $NaNO_3$ gave the highest efficiency (94%) due to enhanced adsorption and $^{\bullet}OH$ generation *via* photolysis, while $CaCl_2$ showed the lowest, as Ca^{2+} binding suppressed NC surface charge and dye interaction. Salt type

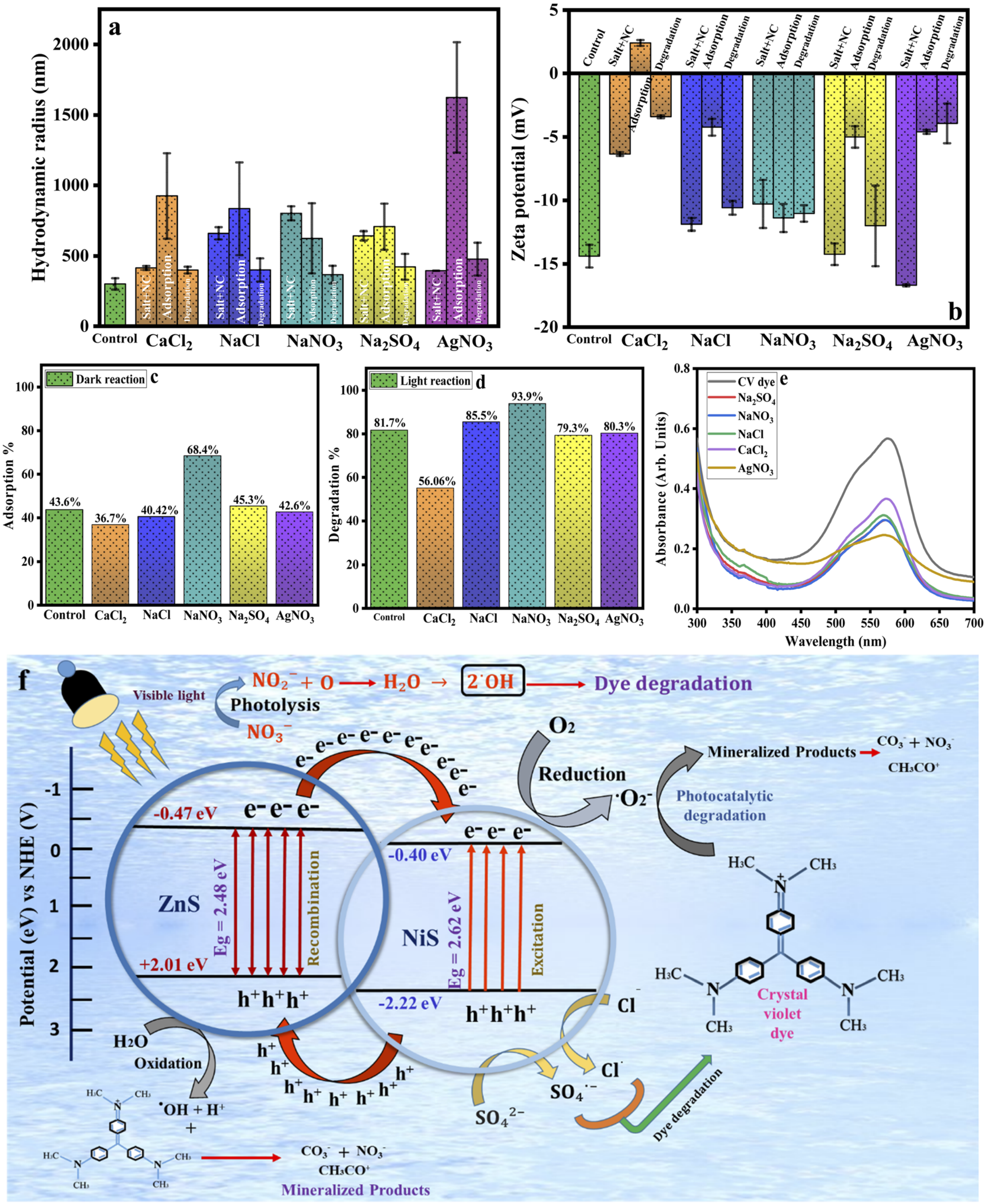

Fig. 11 (a) H_R of NC in salt after dye adsorption and photocatalytic degradation; (b) ζ potential of NC in various salts after dye adsorption and photocatalytic degradation (salt centration: 0.1 M, CV concentration: 20 mg L^{-1}, dose: 0.2 g L^{-1}, pH: 6.9); effect of inorganic salts on (c) adsorption and (d) photodegradation efficiency of NC (CV concentration: 20 mg L^{-1}, dose: 0.2 g L^{-1}, salt concentration: 0.1 M, pH: 6.9); (e) UV-Vis spectra of the control studies of salts (CV concentration: 10 mg L^{-1}, salt concentration: 0.1 M, irradiation time: 60 min); and (f) charge-transfer mechanism in the NiS–ZnS NC and the role of salt anions in dye degradation.

thus plays a decisive role in photocatalytic performance. Eqn (S1)–(S6) express the generation of hydroxyl radicals by nitrate ions.[97] It is also consistent with the literature, as the generation of oxygen radicals from nitrate ions gives rise to hydroxyl radicals that participate in dye degradation. The generation of such radicals is given by eqn (S7)–(S9).[98]

Enhanced photocatalytic activity was observed only with $NaNO_3$, which increased CV adsorption and generated $^{\bullet}OH$ radicals *via* photolysis (Fig. 11a–d). In contrast, $AgNO_3$, despite sharing the same anion, reduced both adsorption and degradation due to competition of Ag^+ with CV for surface sites, lower surface charge, and electron scavenging by Ag^+. $CaCl_2$ further suppressed efficiency to 55%, as Ca^{2+} strongly neutralized the NC surface charge, weakening dye interaction; ζ potential shifted from 2.40 ± 0.23 to −3.40 ± 0.12 mV after degradation, indicating incomplete recovery due to Ca^{2+} deposition (Fig. 11b). Monovalent Na^{+} caused a lower degree of surface neutralization than divalent Ca^{2+}.[99] In NaCl, degradation reached 85.5%, with surface charge decreasing from −14.3 ± 1.0 to −4.23 ± 0.67 mV and H_R rising from 300 ± 46.7 to 834 ± 329 nm after adsorption, as shown in Fig. 11a and b. Following degradation, the ζ potential recovered to −10.6 ± 0.55 mV, and H_R declined to 400 ± 82.5 nm, confirming efficient degradation assisted by reactive chlorine species, eqn S10 and S11).[33,100,101]

For Na_2SO_4, the ζ potential of the NiS–ZnS NC decreased slightly from −14.4 ± 0.9 to −14.0 ± 0.85 mV, while the H_R increased to 642 ± 33 nm, suggesting minimal interaction of Na^{+} cations and a more pronounced role of SO_4^{2-} anions (Fig. 11a and b). This led to modestly enhanced CV adsorption (45.3%, Fig. 11c), largely due to the preservation of NC's negative surface charge. Upon dye adsorption, the surface charge decreased further and H_R increased, confirming favorable electrostatic binding between the cationic dye and NC. After photocatalytic degradation, the ζ potential recovered toward more negative values and H_R decreased, consistent with successful dye removal. However, the overall degradation efficiency (79.8%) remained lower than that in other salt systems. This reduction is attributed to the quenching effect of SO_4^{2-} anions, which can simultaneously scavenge valence-band holes and conduction-band electrons, thereby suppressing radical formation and limiting photocatalytic activity.[102] Generation of sulfate radicals, eqn (S12) and (S13).

Sulfate radicals are less effective than hydroxyl radicals ($^{\bullet}OH$), due to their large size, and the radical function could be distributed over a resonance structure, which may render them less effective than hydroxyl radicals in dye degradation. However, their inhibitory effect may be low due to their oxidizing ability for organics.[97]

Control studies of salts

To examine the effects of salt, dye solutions containing 0.1 M of each salt were irradiated for 60 min under identical conditions (Fig. 11e). Chloride salts showed the highest removal efficiency,

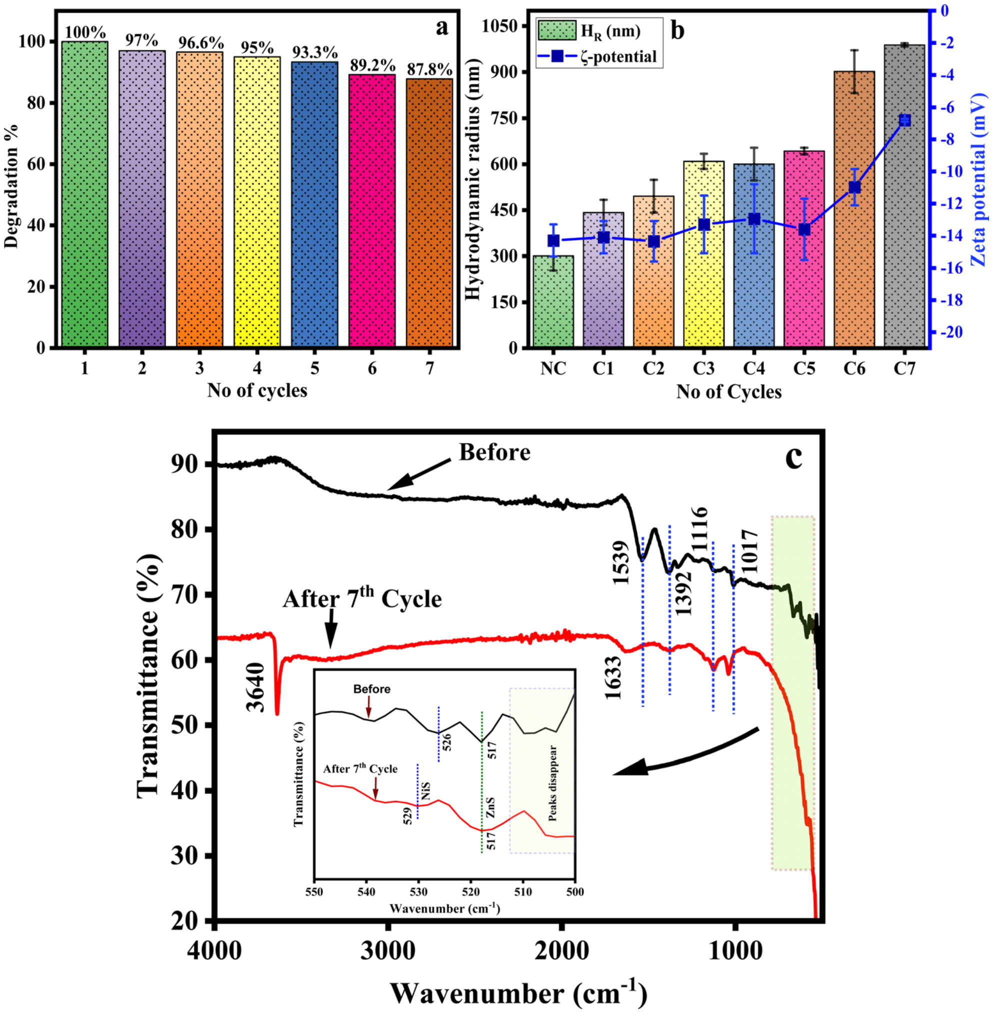

Fig. 12 (a) Photocatalytic degradation cycles (dose: 3 g L^{-1}, CV concentration: 30 mg L^{-1}, pH: 6.9); (b) recyclability and stability (CV concentration: 30 mg L^{-1}, T: 20 °C, dose: 2 g L^{-1}, pH: 6.9); and (c) FTIR spectra of the NiS–ZnS NC before and after the 7th cycle of photocatalytic degradation.

nitrate salts the lowest, and sulfate salts exhibited an intermediate effect. The high removal efficiency of chloride ions can be associated with the generation of reactive species ($Cl^•$, $Cl_2^{•-}$, Cl_2, and HClO) by the action of chloride ions with hydroxyl radicals, which degrade dye molecules. The generation of such active species can be expressed using eqn (S14)–(S19).[103]

The effect of nitrate salts has also been investigated, which results in the generation of hydroxyl radicals by nitrate ions in light, eqn (S1)–(S9).

Effect of sulfate ions on control salt studies

A study reported the production of active sulfate radicals from sodium persulfate (NaS_2O_8) when exposed to light. Such an active species acts as an oxidizing agent, which attacks dye molecules and causes their elimination from the aqueous medium,[104] eqn (S12) and (S13).

The adsorption and photocatalytic efficiency of the nanocomposite in various salts decrease in the following order: $NaNO_3$ > control > Na_2SO_4 >$AgNO_3$ > NaCl > $CaCl_2$ and $NaNO_3$ > control > NaCl > $AgNO_3$ > NaCl > Na_2SO_4 > $CaCl_2$.

Photocatalytic mechanism of NC in salts

In the NiS–ZnS nanocomposite (NC), NiS acts as a p-type semiconductor and electron acceptor, reducing surface-charge effects and prolonging the lifetime of photogenerated carriers. At the same time, ZnS functions as an n-type semiconductor with electron-donating properties. UV-vis and PL analyses confirm that both materials are visible-light active and promote charge separation during photocatalysis. Under irradiation, the electrons (e^-) in the conduction band (CB) of ZnS are efficiently transferred to the CB of NiS,[34] where they reduce dissolved O_2 molecules to generate superoxide radicals ($^•O_2^-$). Concurrently, holes (h^+) formed in the valence band (VB) of NiS are transferred to the valence band (VB) of ZnS, where they oxidize water molecules, producing hydroxyl radicals ($^•OH$). These reactive species not only degrade the dye molecules adsorbed on the NC surface but also diffuse into the bulk solution, driving mineralization into CO_2 and H_2O,[105] as confirmed from the LC-MS data given in (Fig. S5). Salts further influence the charge-transfer process by generating additional radicals. Chloride and sulfate ions capture VB holes to form $Cl^•$ and $SO_4^{•-}$ species, while nitrate (NO_3^-) undergoes photolysis to nitrite (NO_2^-), producing $^•OH$ radicals, as mentioned in Fig. 11f. Collectively, these processes accelerate photocatalytic degradation, as illustrated in Fig. 11e.

The conduction band (CB) and valence band (VB) edge positions of NiS and ZnS were estimated using the Mulliken electronegativity approach (eqn (9) and (10)):[106]

$$E_{CB} = X - E_e - 0.5E_g \tag{9}$$

$$E_{VB} = E_{CB} + E_g \tag{10}$$

where X is the absolute electronegativity, E_e is the energy of free electrons on the hydrogen scale (4.5 eV), and E_g is the experimentally measured band gap. Based on these calculations, ZnS (n-type) shows CB and VB positions of −0.47 eV and +2.01 eV *vs.* NHE, respectively, whereas NiS (p-type) shows CB and VB positions of −0.40 eV and +2.22 eV *vs.* NHE (Fig. 11f). This band alignment results in the formation of a p-n heterojunction, enabling the transfer of photogenerated electrons (e^-) from the CB of ZnS to that of NiS, while holes (h^+) migrate from the VB of NiS to the VB of ZnS. Such directional charge transfer promotes efficient charge separation, suppresses e^-/h^+ recombination, and consequently augments photocatalytic activity.[58]

Table 2 Comparison of the photocatalytic activity of the NiS–ZnS NC with that of different nanomaterials for the photocatalytic degradation of different dyes

S. No	Nanomaterials	Source	Time (min)	Experimental conditions	Degradation (%)	References
1	CdS and Cu@CdS nanoparticles	Visible light	15	Concentration: 100 mg L^{-1}, dose: 200 mg	98.88	108
2	CuS-CNTs	Visible light	90	Methylene blue concentration: 15 mg L^{-1}, dose: 15 mg	100	109
3	CuS/CdS Z-scheme	Visible light	48	Trypan blue concentration: 15 mg L^{-1}, dose: 20 mg	81	110
4	Ag_2O–V_2O_5 nanocomposite	UV-vis light	120	Concentration: 10 mg L^{-1}, dose: 10 mg	92.3	111
5	Sn-doped ZnS NPs	Visible	120	Concentration: 20 mg L^{-1}, dose: 25 mg	95	112
6	In_2MnS_4 micro-flowers	300 W Xe lamp	100	Concentration: 5 mg L^{-1}, dose: 100 mg	96.6	113
7	ZnS/rGO/g-C_3N_4	Visible light	70	Concentration: 25 mg L^{-1}, dose: 10 mg	96.7	114
8	Copper zinc tin sulfide (CZTS)-MoS_2	300 W halogen lamp	80	Concentration: 20 mg L^{-1}, dose: 20 mg	79.9	115
9	Zn-doped and (Y, Zn)-*co*-doped CeO_2/CdS heterostructures	UV-vis light	120	Concentration: 1, 2, and 3 mg L^{-1}; dose: 3 mg	100	116
10	NiS–ZnS NC	Visible light (halogen lamp-500 W)	60	Concentration: 20 mg L^{-1}, dose: 40 mg	98	Present study

Recyclability and structural stability analysis by DLS and FTIR spectroscopy

Recyclability and stability. The durability of the NC was evaluated across seven successive photocatalytic cycles (Fig. 12a). The catalyst retained nearly complete activity, degrading 100% of CV in the first cycle and 97% in the second, with only a gradual decline thereafter. By the seventh cycle, efficiency decreased modestly due to partial loss of colloidal stability. Such losses can be attributed to the deposition of organic acetyl cation (CH_3CO^+) and inorganic nitrate (NO_3^-) and sulfate (SO_4^{2-}) anion on the photocatalyst surface that can affect the particle diffusion speed by changing the thickness of the electric double layer called the Debye length (K^{-1}). Thus, a low-conductivity medium forms an extended ionic double layer around the particle, thereby slowing diffusion and leading to a larger apparent hydrodynamic diameter.[38,107] DLS measurements confirmed this trend: H_R increased progressively up to the fifth cycle, while the ζ potential showed a corresponding decline, indicating aggregation (Fig. 12b). Beyond the fifth cycle, agglomeration became more pronounced, reducing the effective surface area available for dye interaction and accounting for the reduced photocatalytic efficiency observed in later cycles. Nonetheless, the NC demonstrated excellent stability, maintaining high activity over repeated use.[33]

The FTIR spectra showed nearly no changes after recycling (Fig. 12c), confirming the material's structural stability. However, a slight change was observed in the 500–540 cm^{-1} region, where the peaks at 503 and 509 cm^{-1} disappeared (Fig. 12c, inset). The peaks at 517 and 529 cm^{-1} remained intact, confirming the presence of ZnS and NiS entities in the nanocomposite, respectively, consistent with Fig. 12c (inset) and Fig. 4d. Overall, the FTIR spectra before and after the 7th cycle are nearly identical (Fig. 12c), with only a minor decrease in intensity, confirming the structural stability and good reusability of the NiS–ZnS NC for potential industrial applications.

Comparison of photocatalysts. The photocatalytic performance of the NiS–ZnS NC towards CV dye, as summarized in

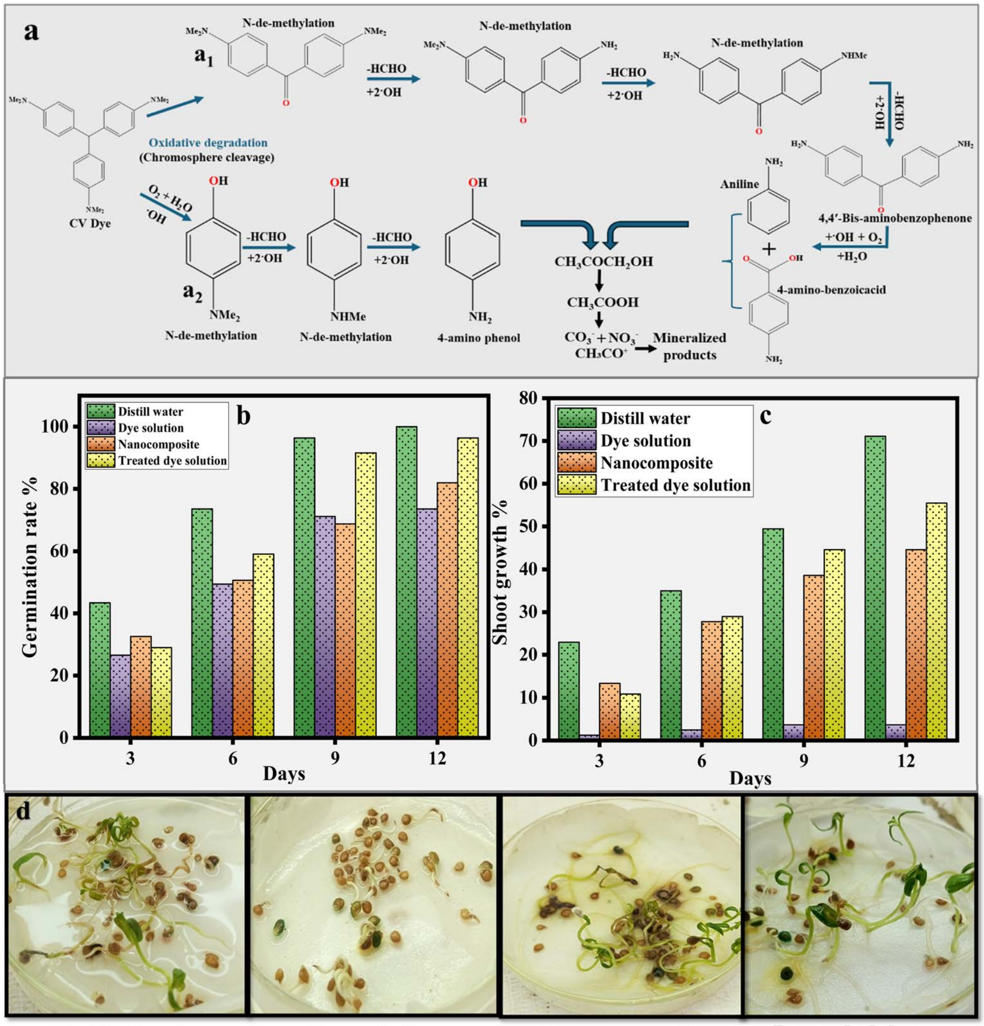

Distilled water Dye solution Nanocomposite Degraded dye solution

Fig. 13 (a) Proposed mechanism of cleavage of the crystal violet dye structure *via* the photocatalytic degradation pathway, and growth of tomato seeds after 12 days of germination under different treatments: (b) germination rate (%), (c) shoot growth, and (d) images of germinated seeds.

Table 2, demonstrates its superior efficiency compared to recently reported photocatalysts. The NC exhibits remarkable stability and reusability, sustaining a high degradation efficiency even after the 7th cycle. These findings highlight its robustness, consistency, and strong potential for practical wastewater-treatment applications.

Possible photocatalytic degradation pathway and phytotoxicity study for the crystal violet dye

Theoretical investigations also validated the possible interaction of NC with the C1 (branched nitrogen atom) and C2 positions (aromatic rings) of CV, with more pronounced interaction at the C2 position, also responsible for the reduction in the band gap of NC (Fig. 10). This feasible interaction is further supported by the electrostatic attraction between the negatively charged NC surface (Fig. 7b) and the cationic CV dye, which carries a positively charged dimethylene group.

The degradation products of the CV dye (*N*,*N*,*N*,*N*,*N*,*N*-hexaethylpararosaniline), identified from LC-MS spectra (Fig. S5), include possible intermediates listed in Table S2. The degradation products detected are relevant to the literature.

The photocatalytic degradation of CV proceeded *via* an initial $^{\bullet}$OH-induced oxidative cleavage at the central carbon of the amino-triphenylmethane chromophore, generating smaller aromatic intermediates, (a_1) 4-(*N*, *N*-dimethylamino)-4′–(*N*′,*N*′-dimethylamino) benzophenone and (a_2) 4-*N*, *N* (dimethyl amino) phenol, mentioned in the mechanism.[117] After CV cleavage, the subsequent *N*-demethylation of intermediate (a_1) occurs through the attack of $^{\bullet}$OH radicals and the removal of the formyl group. Hydroxyl radicals are formed directly from the reaction of holes with surface-adsorbed water or $^{\bullet}$OH radicals. Intermediate (a_1) results in two degradation products, 4-aminobenzoic acid and aniline at the end, which further degrade into carbonates, nitrates, acetyl cation, and finally the mineralized products CO_2 and H_2O.[100] The second intermediate, (a_2) 4-*N*,*N* (dimethyl amino) phenol, also undergoes subsequent *N*-demethylation in the presence of hydroxyl radicals. This leads to the removal of formyl groups, yielding intermediate 4-aminophenol, which further degrades into 1-hydroxypropan-2-one, followed by acetic acid, acetyl cations, and the final mineralized products. LC-MS data confirmed the complete mineralization of crystal violet, yielding CO_2 and H_2O as the final products (Fig. 13a and S5).

Phytotoxicity and germination studies

The phytotoxicity of treated and untreated dye solutions, as well as the NiS–ZnS NC suspension, was evaluated using tomato-seed germination tests. In the control environment, 100% germination was observed with normal shoot growth. Seeds exposed to the treated dye solution showed 96% germination and 55% shoot growth, indicating substantially reduced toxicity after photocatalytic treatment. The NC suspension demonstrated 81% germination with 44% shoot growth, confirming the material's biocompatibility. By contrast, seeds exposed to the untreated dye solution exhibited only 73% germination and severely stunted shoot growth (3%), highlighting the inherent toxicity of crystal violet (Fig. 13b and c).

These results align with previous reports by Hussain *et al.* and Mohamed *et al.*.[118,119] The representative images of seed germination under different conditions are given in Fig. 13d.

Conclusion

This study focuses on synthesizing pure NiS, ZnS, and an optimized NiS–ZnS NC *via* a co-precipitation method. Parameters, including the precursor concentration, pH, temperature, stabilizer content, and reactant addition rate, were optimized for controlling the H_R (300 ± 46.7 nm), PdI (0.42 ± 0.20), and ζ potential (−14.4 ± 0.9 mV) of the NiS–ZnS NC. These parameters were tuned across different pH values and inorganic salts for effective dye interaction and were systematically evaluated by DLS. XRD, SEM, TEM, EDX, and XPS confirmed the successful formation of the NiS–ZnS NC with ∼1.98 nm crystallite size and an agglomerated morphology, and Ni–Zn–S elemental signatures were consistent with those of the well-defined Ni^{2+} and Zn^{2+} sulfide phases. DLS and FTIR analyses confirmed the stability of NC in dispersion based on the H_R and surface charge. Further, it exhibited structural stability up to the 7th cycle, maintaining 87.8% removal efficiency, highlighting its practical applicability. BET confirm its mesoporous nature with surface area (65.3 $m^2\ g^{-1}$), pore volume, and pore diameter (0.141 $cm^3\ g^{-1}$, 0.563 nm) measurements. UV-Vis and PL results confirm the NC formation with a band gap of 2.57 eV (making it visible light active), indicating the suppression of e^-/h^+ recombination through the heterojunction.

Photocatalytic testing across various anionic and cationic dyes demonstrated the effective nature of NC for cationic-dye degradation, achieving 98% removal of CV under favorable alkaline conditions. DLS revealed the role of NC interactions with monovalent and divalent ions in tuning its surface charge and H_R, thereby regulating dye adsorption and photocatalytic degradation. Specifically, $NaNO_3$ enhances, while $CaCl_2$ suppresses, the dye degradation efficiency; these processes provide novel mechanistic insights into ion-mediated photocatalysis. Complementary DFT, DOS, and NCI analyses confirmed the band gap narrowing, strong dye–NC binding, and favorable charge-transfer interactions that underpin the NC's photocatalytic activity. A toxicity study reveals the environmentally friendly nature of NC and the treated CV solution. Collectively, these results establish NiS–ZnS as a robust, stable, tunable, and visible light-active photocatalyst with strong potential for practical wastewater-treatment applications, both in the absence and presence of salt systems.

Conflicts of interest

The authors declare that they have no competing interests.

Data availability

The data supporting the findings of this study are available within the article and its supplementary information (SI).

Additional experimental and computational data are available from the corresponding author upon reasonable request. Supplementary information is available. See DOI: https://doi.org/10.1039/d6ra01846g.

Acknowledgements

The authors acknowledge the Deanship of Scientific Research, Vice Presidency for Graduate Studies and Scientific Research, King Faisal University, Saudi Arabia (Grant No. KFU267979). This work was supported by the Deanship of Scientific Research, Vice Presidency for Graduate Studies and Scientific Research, King Faisal University, Saudi Arabia [Grant No. KFU261892].

References

1 Z. Iqbal, K. Zia and A. Ahmad, Pesticide abuse in Pakistan and associated human health and environmental risks, *Pak. J. Agric. Sci.*, 1997, **34**, 94–97.

2 H. U. Rehman and F. Nadeem, Analysis of land and water degradation, its drivers, and remedial strategies for south Punjab, Pakistan, *Sci. Rec.*, 2025, **2**, 28–37.

3 M. Hussain, *Impact of Wastewater on the Soil–Plant–Atmosphere Interface: Challenges and Remediation Approaches Science & Society Insights*, 2025, vol. 1, pp. 25–33.

4 S. A. Aijaz, Z. Shafi and M. Shahid, Magnetized phyto-adsorbents for industrial dye removal: functionalization and mechanistic insights for sustainable wastewater remediation, *RSC Adv.*, 2026, **16**, 758–777.

5 H. Isawi, E. M. Ahmed, M. Rabee and H. Moustafa, Using natural antioxidant Rhubarb extracts in PVA/chitosan bio-adsorbent films for efficient removal of cationic and anionic dyes from polluted water, *J. Ind. Eng. Chem.*, 2025, **141**, 626–644.

6 M. Shahzaib, M. Usman, M. U. Rahman, M. A. S. Khan, M. N. Zulfiqar and I. Yaseen, Nanoparticles: Concept, types and applications in engineering technology (water treatment, energy production and biomedical technology), *Sci. Soc. Insights*, 2025, **205**(4), 79–84.

7 S. Mohanty, S. Moulick and S. K. Maji, Adsorption/photodegradation of crystal violet (basic dye) from aqueous solution by hydrothermally synthesized titanate nanotube (TNT), *J. Water Proc. Eng.*, 2020, **37**, 101428.

8 R. M. M. Muhsin, T. S. B. Abd Manan, J. Bidai, M. S. A. Mangat, Z. M. Hanafiah, A. Gohari, N. Ahmad, F. Ahmad, S. Beddu and N. L. M. Kamal, Polycyclic aromatic hydrocarbons (PAHs) occurrences in water bodies, extraction techniques, detection methods, and standardized guidelines for PAHs in aqueous solutions, *Sci. Total Environ.*, 2025, **972**, 179123.

9 J. Wu, Q. Li, W. Li, Y. Li, G. Wang, A. Li and H. Li, Efficient removal of acid dyes using permanent magnetic resin and its preliminary investigation for advanced treatment of dyeing effluents, *J. Clean. Prod.*, 2020, **251**, 119694.

10 W. Saeed, Z. Abbasi, M. Bilal, S. H. Shah, A. Waseem and A. J. Shaikh, Interactive behavior of graphene quantum dots towards noble metal surfaces, *Phys. E*, 2023, **147**, 115596.

11 Z. Zhou, Y. Yao, Y. Yang, X. Li, J. Ren and J. Qin, Ultrasound-assisted H_2O_2 directional-modification of powdered activated carbon for the enhanced adsorption of secondary effluent organic matter from printing and dyeing processes, *J. Hazard. Mater.*, 2023, **449**, 131065.

12 A. Ranjbari, A. P. Anbari, M. Kashif, K. K. Adhikary, K.-H. Kim and P. M. Heynderickx, The adsorption/photocatalytic degradation kinetics of oxygen vacancy-enriched ZnO in relation to surface functional groups of cationic/anionic dyes, *Chem. Eng. J.*, 2025, **505**, 159526.

13 Z.-C. Fu, Y. Qin, H.-J. Yang, W.-L. An, T. Wang, J.-N. Deng and M.-J. Chen, Photocatalytic radical (O) P–P (O) bond formation: access to diphosphine dioxides for thermoset protection, *Green Chem.*, 2026, **28**, 4602–4609.

14 B. Zhou, J. J. Wang, P. Dangal, S. Lomnicki, A. D. Roy and J.-H. Park, A novel sugarcane residue-derived bimetallic Fe/Mn-biochar composite for activation of peroxymonosulfate in advanced oxidation process removal of azo dye: Degradation behavior and mechanism, *J. Water Proc. Eng.*, 2024, **58**, 104740.

15 Y. Du, J. Yu, B. Chen and X. Zhu, Recent progresses in the modification strategies of MXene-based membranes for water and wastewater treatments, *Environ. Sci.: Nano*, 2025, **12**, 150–188.

16 A. Asghar, M. I. Yousaf, N. A. Shad, M. Munir Sajid, A. M. Afzal, Y. Javed, A. Razzaq, M. Shariq, Q.-u.-a. Gulfam and M. Sarwar, Enhanced electrochemical performance of hydrothermally synthesized NiS/ZnS composites as an electrode for super-capacitors, *J. Cluster Sci.*, 2022, **33**, 2325–2335.

17 A. Ullah, M. R. Khawar, N. A. Shad, S. Jang, D. Choi, D. Geng, J. Shahbaz, A. M. Tighezza, Y. Javed and A. Ahmad, Zinc/lead bimetallic sulfides as hybrid material for high-performance aqueous asymmetric supercapacitor and photocatalytic degradation of organic dye, *J. Alloys Compd.*, 2025, **1010**, 177565.

18 R. Rajendran, M. Alsawalha, T. Alomayri, P. Arumugam, P. Matheswaran, T. H. Oh, S. Suganthi and T. Rojviroon, Optimized MoS_2/SnS_2@ AC nanocomposites for superior visible light-driven pollutant degradation and antibacterial activity, *Inorg. Chem. Commun.*, 2025, **173**, 113839.

19 S. Thangavel, K. Krishnamoorthy, S.-J. Kim and G. Venugopal, Designing ZnS decorated reduced graphene-oxide nanohybrid via microwave route and their application in photocatalysis, *J. Alloys Compd.*, 2016, **683**, 456–462.

20 Z. M. Aldhafeeri, M. Aadil, S. Mubeen, A. Khalid, M. R. El-Aassar, M. Hasan, M. Algarni and M. R. Alrahili, Synthesis of assembled Ag-Bi_2O_3/rGO composites using hydrothermal and ultrasonication and its application in drug and dye annihilation, *Ceram. Int.*, 2025, **51**, 27912–27924.

21 Y. Lei, J. Liang, L. Chen, S. Jin, D. Tang and B. Xi, Magnetically induced S-doped g-C3N4 to form interfacial

SS bonds and abundant S vacancies synergistically endow S-doped-C_3N_4/ZnCdS: Oriented conversion of HMF to FDCA and hydrogen evolution, *Chem. Eng. J.*, 2025, 168948.

22 Y. Zheng, Y. Liu, X. Guo, Z. Chen, W. Zhang, Y. Wang, X. Tang, Y. Zhang and Y. Zhao, Sulfur-doped g-C_3N_4/rGO porous nanosheets for highly efficient photocatalytic degradation of refractory contaminants, *J. Mater. Sci. Technol.*, 2020, **41**, 117–126.

23 F. Jamal, A. Rafique, S. Moeen, J. Haider, W. Nabgan, A. Haider, M. Imran, G. Nazir, M. Alhassan and M. Ikram, Review of metal sulfide nanostructures and their applications, *ACS Appl. Nano Mater.*, 2023, **6**, 7077–7106.

24 M. O. Qamar and Y.-H. Ahn, Key parameters for enhancing visible-light-driven photocatalytic activity of ZnS nanoparticle, *J. Clean. Prod.*, 2023, **420**, 138374.

25 S. Wang, X. Niu, L. Wang, J. Bi, W. Yang and H. Hou, Recent advances in non-metal doped ZnS nanostructures for photocatalytic hydrogen production, *Microstructures*, 2025, **5**, 2025074.

26 M. Ahmad, S. Rasool, F. Khitab, N. Ahmad, F. Ahmad, A. S. Khan and N. Jamila, Nickel-impregnated ZnO catalysts: a promising catalyst for efficient methylene blue dye degradation via photocatalysis and sonocatalysis, *Environ. Sci. Pollut. Res.*, 2025, **32**, 23054–23067.

27 A. Raza, H. Noor and S. Riaz, Structural, Optical, and Photocatalytic Properties of Ni-Doped ZnS Nanoparticles, *ChemistrySelect*, 2025, **10**, e05710.

28 I. Shakoor, U. Jabeen, I. Ahmad, S. Riaz, M. Tayyab, A. Syed, A. H. Bahkali, M. Riaz, R. R. Zairov and M. N. Zafar, ZnS and Fe-doped ZnS photocatalysts for improved visible light driven photocatalytic degradation of methylene blue, *Inorg. Chim. Acta*, 2024, **560**, 121837.

29 Z. Jiao, X. Shuai, Y. Du and J. Du, Combining crystal planes and heterojunctions of ZnS/SnS_2 boosts photocatalytic performance, *J. Chem. Phys.*, 2025, 162.

30 R. Mandam, H. B. Boppudi, C. Kuchi, M. C. Sekhar, P. Chandrasekar, M. Jagadeesh, A. A. Ansari, N. P. Reddy and P. S. Reddy, A hydrothermally engineered MoS_2–ZnS–MWCNT nanocomposite for superior oxygen evolution and visible light photocatalytic dye degradation, *J. Mater. Sci.*, 2026, 1–17.

31 X. Zheng, Y. Dong and T. Liu, Simultaneous photodegradation of dyes by NiS/CuS-CdS composites in visible light region, *Colloids Surf., A*, 2020, **598**, 124854.

32 X. Liu, X. Liang, P. Wang, B. Huang, X. Qin, X. Zhang and Y. Dai, Highly efficient and noble metal-free NiS modified MnxCd1-xS solid solutions with enhanced photocatalytic activity for hydrogen evolution under visible light irradiation, *Appl. Catal., B*, 2017, **203**, 282–288.

33 M. Y. Afzal, M. Bilal, H. Khan, M. Asif, M. S. Khan, M. Iqbal, T. A. Butt, M. Hassan and A. J. Shaikh, Understanding Photocatalytic Degradation of RB5 Dye under Salts Using Nickel Sulfide Nanoparticles: Insights from Dynamic Light Scattering and Theoretical Investigations, *ACS Omega*, 2025, **10**, 32918–32938.

34 V. Alagarsamy, N. Venkatesh, S. A. Roshan, S. Pandurengan, L. Gnanasekaran, K. Viswanathan and G. Murugadoss, NiS-ZnS quantum dots as visible-light photocatalysts for enhanced dye degradation in sustainable wastewater treatment, *Chem. Phys. Impact*, 2025, 100912.

35 J. Zou, L. Li, N. Tan, K. Zhang, L. Wang and Z. Chen, Construction of S-scheme heterojunction with interfacial chemical bonds for enhanced photocatalytic CO_2 reduction, *Appl. Surf. Sci.*, 2025, 165001.

36 H. U. Rehman, H. Khan, Z. Abbasi, L. B. Tahar, R. A. Khan, A. Waseem and A. J. Shaikh, DLS-based optimization of ZnS–CoS nanoparticles with enhanced energy and power density for supercapacitor applications and its validation by AI models, *Mater. Adv.*, 2025, **6**, 7847–7865.

37 A. Khanum, S. Ajaib, H. U. Rehman, Z. Abbasi, A. Waseem, L. B. Tahar, F. Shah and A. J. Shaikh, Rational Optimization of NiS-CoS Composite Nanoparticles via Controlled Co-Precipitation for High-Efficiency Supercapacitors, *New J. Chem.*, 2026, **50**, 6780–6800.

38 P. Borthakur and M. R. Das, Hydrothermal assisted decoration of NiS_2 and CoS nanoparticles on the reduced graphene oxide nanosheets for sunlight driven photocatalytic degradation of azo dye: Effect of background electrolyte and surface charge, *J. Colloid Interface Sci.*, 2018, **516**, 342–354.

39 J. Wang and S. Wang, Effect of inorganic anions on the performance of advanced oxidation processes for degradation of organic contaminants, *Chem. Eng. J.*, 2021, **411**, 128392.

40 Y. Miyah, A. Lahrichi, M. Idrissi, S. Boujraf, H. Taouda and F. Zerrouq, Assessment of adsorption kinetics for removal potential of Crystal Violet dye from aqueous solutions using Moroccan pyrophyllite, *J. Assoc. Arab Univ. Basic Appl. Sci.*, 2017, **23**, 20–28.

41 R. Rai, A. George, V. Sai Muthukumar, K. Varma, R. Philip and M. Molli, Investigation of nonlinear optical and photocatalytic properties of sol–gel derived $KBiFe_2O_5$, *J. Mater. Sci.: Mater. Electron.*, 2019, **30**, 11451–11457.

42 M. Hussain, M. Aadil, E. W. Cochran, S. Zulfiqar, W. Hassan, T. Kousar, H. Somaily and F. Mahmood, Facile synthesis of a porous sorbent derived from the rice husk biomass: a new and highly efficient material for water remediation, *Inorg. Chem. Commun.*, 2024, **160**, 112010.

43 M. S. Khan, N. Riaz, S. Rehman, L. Chenhui, A. J. Shaikh, M. Arfan, I. Zeb, M. Arshad, F. Hafeez and M. Bilal, Improved photocatalytic decolorization of reactive black 5 dye through synthesis of graphene quantum dots–nitrogen-doped TiO_2, *Environ. Sci. Pollut. Res.*, 2023, **30**, 124992–125005.

44 D. Huang, M. Wen, C. Zhou, Z. Li, M. Cheng, S. Chen, W. Xue, L. Lei, Y. Yang and W. Xiong, ZnxCd1-xS based materials for photocatalytic hydrogen evolution, pollutants degradation and carbon dioxide reduction, *Appl. Catal., B*, 2020, **267**, 118651.

45 F. Amiri, S. Saeednia and P. Iranmanesh, Synthesis and investigation of properties of bismuth sulfide nanoparticles by solvothermal method, *Discov. Chem.*, 2026, **3**, 85.

46 A. J. W. Frisch, *25p, Gaussian 09W Reference*, USA, 2009, p. 470.

47 Y. Choi, B. J. Park, Y. Lee, K. S. Lee, J. K. Kim and J. W. Han, Synergistic Fe, Pd diatomic sites anchored on porous nitrogen-doped carbon for efficient oxygen reduction in the entire pH range, *J. Mater. Chem. A*, 2025, **13**(27), 21462–21471.

48 Y. Jeong, D. W. Lim and J. Choi, Assessment of size-dependent antimicrobial and cytotoxic properties of silver nanoparticles, *Adv. Mater. Sci. Eng.*, 2014, **2014**, 763807.

49 A. H. Shah and M. A. Rather, Effect of calcination temperature on the crystallite size, particle size and zeta potential of TiO_2 nanoparticles synthesized via polyol-mediated method, *Mater. Today: Proc.*, 2021, **44**, 482–488.

50 M. Kasture, P. Patel, A. Prabhune, C. Ramana, A. Kulkarni and B. Prasad, Synthesis of silver nanoparticles by sophorolipids: Effect of temperature and sophorolipid structure on the size of particles, *J. Chem. Sci.*, 2008, **120**, 515–520.

51 G. Muralidharan, L. Subramanian, S. K. Nallamuthu, V. Santhanam and S. Kumar, Effect of reagent addition rate and temperature on synthesis of gold nanoparticles in microemulsion route, *Ind. Eng. Chem. Res.*, 2011, **50**, 8786–8791.

52 S. Bhattacharjee, DLS and zeta potential–what they are and what they are not?, *J. Control. Release*, 2016, **235**, 337–351.

53 L. Mahmudin, E. Suharyadi, A. B. S. Utomo and K. Abraha, Influence of stabilizing agent and synthesis temperature on the optical properties of silver nanoparticles as active materials in surface plasmon resonance (SPR) biosensor, *AIP Conf. Proc.*, 2016, **1725**(1), 020041.

54 M. Ovissipour, S. M. Roopesh, B. A. Rasco and S. S. Sablani, Engineered nanoparticles (ENPs): Applications, risk assessment, and risk management in the agriculture and food sectors, *Food Chemical Hazard Detection: Development and Application of New Technologies*, 2014, pp. 207–247.

55 M. Elbehary, Y. A. Dowidar, A. M. Ashour, E. M. A. El-Fattah and A. Monir, Effect of in vitro maturation medium supplementation with chitosan nanoparticles on the river buffalo cumulus-oocyte complexes, *Int. J. Vet. Sci.*, 2023, **12**, 341–346.

56 Y.-L. Liu, P. Cao, Q. Zhang, C. Guo, J. Li and Q. Zeng, Solar-activated ZnS@ MXene heterostructure for integrated radioactive wastewater treatment and energy harvesting, *Water Res.*, 2025, 124254.

57 A. B. Alwany, G. Youssef, E. E. Saleh, O. Samir, M. A. Algradee and A. Alnehia, Structural, optical and radiation shielding properties of ZnS nanoparticles QDs, *Optik*, 2022, **260**, 169124.

58 F. Amiri, P. Iranmanesh, N. Khorasanipour and S. Saeednia, Detailed investigation of the optical and photocatalytic properties of ZnS/NiS nanocomposite for efficient water purification and dye degradation, *Int. J. Environ. Sci. Technol.*, 2026, **23**, 48.

59 N. C. Ramgopal, G. Sreedevi, S. Majumder, S. Alhammadi, R. A. Alshgari, M. Mushab, S. K. Arla, J. S. Kim and S. W. Joo, One-Step hydrothermal synthesis of in-situ constructed NiS rods, mns pebbles, and ZnS nanoflakes (NiS-MnS-ZnS) on ITO for enhanced PEC water splitting, *Fuel*, 2025, **385**, 134177.

60 P. Paunkumar and S. Ganesh Babu, A one-pot synthesis of ZnS-NiS-NiS_2 composite and its synergistic effect on different electrolytes for supercapacitor applications, *J. Solid State Electrochem.*, 2025, **29**, 3967–3976.

61 P. L. Reddy, K. Deshmukh, T. Kovářík, D. Reiger, N. A. Nambiraj, L. R and K. P. SK, Enhanced dielectric properties of green synthesized Nickel Sulphide (NiS) nanoparticles integrated polyvinylalcohol nanocomposites, *Mater. Res. Express*, 2020, **7**, 064007.

62 C. Langa, M. Mathipa, N. Mabuba and N. C. Hintsho-Mbita, Effect of calcination temperature on the structural and photocatalytic properties of nickel sulfide nanoparticles for dye degradation and antibacterial applications, *Chem. Phys. Impact*, 2025, 100913.

63 N. Roushdy, M. S. Elnouby, A. Farag, M. Ramadan, O. El-Shazly and E. El-Wahidy, Structural and electrical characterization of nickel sulfide nanoparticles, *Opt. Quant. Electron.*, 2024, **56**, 1794.

64 N. H. Abdullah, Z. Zainal, S. Silong, M. I. M. Tahir, K.-B. Tan and S.-K. Chang, Synthesis of zinc sulphide nanoparticles from thermal decomposition of zinc N-ethyl cyclohexyl dithiocarbamate complex, *Mater. Chem. Phys.*, 2016, **173**, 33–41.

65 D. Ma, J.-W. Shi, L. Sun, Y. Sun, S. Mao, Z. Pu, C. He, Y. Zhang, D. He and H. Wang, Knack behind the high performance CdS/ZnS-NiS nanocomposites: optimizing synergistic effect between cocatalyst and heterostructure for boosting hydrogen evolution, *Chem. Eng. J.*, 2022, **431**, 133446.

66 J. Wang, S. Liu, P. Song, X. Zhang, Y. Song, W. Guo and Z. Yao, Highly efficient activation of molecular oxygen by Cu@ N doped carbon for antibiotic degradation, *Chem. Eng. J.*, 2025, **507**, 160769.

67 X. Yang, J. Xie, Y. Li, X. Xu, L. Hao, Q. Ran and K. Jia, Amphiphilic polyurethane-assisted uniform dispersion of TiO_2/carbon dots hybrids in amidoximed polyarylene ether membranes for enhanced oil/water separation and photocatalytic organic dye degradation, *Chem. Eng. J.*, 2025, 163841.

68 G. Zhang, J. Li, Z. Wang, X. Xu, T. He, J. Wu and J. Wu, Fabrication of CZS NRs/NiSx NPs hybrids with abundant S-vacancies for signally promoting photocatalytic hydrogen production, *Int. J. Hydrogen Energy*, 2024, **68**, 255–267.

69 Y. Chen, Y. Cheng, T. Zhang, H. Zhang and S. Zhong, Photodeposition of NiS thin film enhanced the visible light hydrogen evolution performance of CdS nanoflowers, *Int. J. Hydrogen Energy*, 2024, **77**, 184–192.

70 M. Shahid, M. Rashed, M. A. Rafea, M. I. Attia, M. R. El-Aassar, A. K. Alanazi, I. Shakir, M. Aadil and M. R. Alrahili, Strategic advances in defect-engineered Ce–Bi_3YO_6/rGO hybrids for rapid crystal violet mineralization under visible illumination, *RSC Adv.*, 2025, **15**, 50324–50336.

71 Y. Fazli, S. M. Pourmortazavi, I. Kohsari, M. S. Karimi and M. Tajdari, Synthesis, characterization and photocatalytic property of nickel sulfide nanoparticles, *J. Mater. Sci.: Mater. Electron.*, 2016, **27**, 7192–7199.

72 S. Nachimuthu, K. Kannan, S. Thangavel and K. Gurushankar, Electrochemical and magnetic properties of 3D porous NiS/CuS nanocomposites, *Appl. Surf. Sci. Adv.*, 2022, **7**, 100209.

73 H. Labiadh, Y. Moualhi, K. Moualhi, A. Othmani and M. Zouaoui, Synthesis of ZnS nanoparticles and the investigation of their structural, optical and electrical properties, *Euro-Mediterr. J. Environ. Integr.*, 2025, **10**, 119–130.

74 K. Chaithra, A. Varghese, T. Vinod and S. D. KR, Multifunctional electrospun membranes incorporated with metal oxide nanoparticles, cellulose acetate, and polyvinylpyrrolidone for wastewater treatment: Oil/water separation, dye adsorption, and dye degradation, *Chem. Eng. J.*, 2024, **499**, 156049.

75 D. Gautam, L. Saya, G. Gambhir and S. Hooda, Enhanced piezocatalytic degradation of cationic dyes using graphene oxide and magnetic beads Nanomaterials: Synthesis, Characterization, and mechanistic insights, *Chem. Eng. J.*, 2024, **498**, 154987.

76 S. Tabasideh, A. Maleki, B. Shahmoradi, E. Ghahremani and G. McKay, Sonophotocatalytic degradation of diazinon in aqueous solution using iron-doped TiO_2 nanoparticles, *Sep. Purif. Technol.*, 2017, **189**, 186–192.

77 A. Mariappan, P. Mannu, T. Thiruppathiraja, T. T. T. Nga, S. Lakshmipathi, C.-L. Dong, R. K. Dharman and T. H. Oh, Interfacial oxygen vacancy modulated ZIF-8-derived ZnO/CuS for the photocatalytic degradation of antibiotic and organic pollutants: DFT calculation and degradation pathways, *Chem. Eng. J.*, 2023, **476**, 146720.

78 M. Saidi, B. A. Reguig, M. El Amine Monir, T. M. Althagafi, M. Fatmi, A. Remil, A. Zehhaf and M. Ghebouli, Kinetics thermodynamics and adsorption study of raw treated diatomite as a sustainable adsorbent for crystal violet dye, *Sci. Rep.*, 2025, **15**, 21991.

79 X. Tian, X. Cai, Z. Zeng, Y. He, X. Xu, L. Lei, C. Xu, X. Xu, Y. Xu and P. Li, Mn doping and core-shell engineering of silane-modified Mn-TiO_2@ SiO_2 nanoparticles with drastically reduced photocatalytic activity for transparent UV-shielding hybrid materials, *Chem. Eng. J.*, 2024, **498**, 155304.

80 K. I. John, T. B. Issa, G. Ho, A. N. Nikoloski and D. Li, Enhanced adsorption and photocatalytic degradation of organics using La-doped g-C3N4 with Ag NPs, *Water Cycle*, 2025, **6**, 151–175.

81 M. S. Khan, N. Riaz, A. J. Shaikh, J. A. Shah, J. Hussain, M. Irshad, M. S. Awan, A. Syed, J. Kallerhoff and M. Arshad, Graphene quantum dot and iron co-doped TiO_2 photocatalysts: Synthesis, performance evaluation and phytotoxicity studies, *Ecotoxicol. Environ. Saf.*, 2021, **226**, 112855.

82 N. Riaz, M. Hassan, M. Siddique, Q. Mahmood, U. Farooq, R. Sarwar and M. S. Khan, Photocatalytic degradation and kinetic modeling of azo dye using bimetallic photocatalysts: effect of synthesis and operational parameters, *Environ. Sci. Pollut. Res. Int.*, 2020, **27**, 2992–3006.

83 L. Ding, Y. Hou, H. Liu, J. Peng, Z. Cao, Y. Zhang, B. Wang, X. Cao, Y. Chang and T. Wang, Alcohols as scavengers for hydroxyl radicals in photocatalytic systems: reliable or not?, *ACS ES&T Water*, 2023, **3**, 3534–3543.

84 T. T. D. Nguyen, D. Nguyen, P. P. Vo, H. N. Doan, H. T. N. Pham, V. H. Hoang, K. T. Le, K. Kinashi, V. T. Huynh and P. T. Nguyen, The roles of ethanol and isopropanol as hole scavengers in the photoreduction reaction of graphene oxide by TiO_2: A competition of oxygenated groups removal and carbon defects invasion, *J. Mol. Liq.*, 2023, **381**, 121831.

85 D. Ma, A. Liu, C. Lu and C. Chen, Photocatalytic dehydrogenation of primary alcohols: Selectivity goes against adsorptivity, *ACS Omega*, 2017, **2**, 4161–4172.

86 X. Liu, W. Ren, W. Song, W. Zhang, Y. Wang, Y. Wang, G. Fan, L. Zhang and Y. Huang, Novel EDTA-chitosan/alginate porous composite beads for the removal of Pb (II) and methylene blue from aqueous solutions, *RSC Adv.*, 2025, **15**, 13728–13743.

87 T. T. D. Nguyen, K. H. Nguyen, L. M. Le, C.-Y. Yeh, M. Yoshimura, H. Van Hoang and P. T. Nguyen, Effects of ethylenediaminetetraacetic acid (EDTA) used as a hole scavenger on UV-assisted photoreduction of graphene oxide on the surface of TiO_2: An investigation of irradiation time and scavenger concentration, *Ceram. Int.*, 2025, DOI: 10.1016/j.ceramint.2025.12.245.

88 G. A. Abelta, L. Al Qadri, M. Febrina, A. Rajak, S. Maulana, M. A. Asagabaldan and T. Taher, Enhanced ammonium adsorption from aqueous solutions using ethylenediaminetetraacetic acid (EDTA) modified lampung (Indonesia) natural zeolite: Isotherm, kinetic, and thermodynamic studies, *Sci. Technol. Indones.*, 2024, **9**, 224–234.

89 Z. Abbas, C. Labbez, S. Nordholm and E. Ahlberg, Size-dependent surface charging of nanoparticles, *J. Phys. Chem. C*, 2008, **112**, 5715–5723.

90 S. Rehman, T. Chen, H. Sun, M. Hanif, T. Peng, O. T. Satti and A. Alshameri, Transforming goethite into high-valent iron active centers on montmorillonite-carbon paired minerals for singlet-oxygen-dominated peroxydisulfate water oxidation, *J. Colloid Interface Sci.*, 2026, 140171.

91 S. Rehman, H. Sun, M. Hanif, T. Peng, X. Tang, O. T. Satti and M. Bilal, Environmentally friendly nitrogen doped paired mineral-carbon for catalytic degradation of diethyl phthalate and crop damage mitigation, *Chem.–Eng. J.*, 2025, **508**, 160321.

92 N. Elboughdiri, I. Lakikza, A. Boublia, S. I. Aouni, N. E. H. Hammoudi, J. Georgin, D. S. P. Franco, H. Ferkous, D. Ghernaout and Y. Benguerba, Application of statistical physical, DFT computation and molecular dynamics simulation for enhanced removal of crystal violet and basic fuchsin dyes utilizing biosorbent derived

from residual watermelon seeds (Citrullus lanatus), *Process Saf. Environ. Prot.*, 2024, **186**, 995–1010.

93 N. Jamila, R. Ullah, F. Khitab, N. Ahmad, F. Ahmad, M. Siddique Afridi, F. Kanwal and N. Khan, Visible-light-sensitive highly-efficient photocatalytic degradation of hazardous contaminant fast yellow AB in industrial wastewater using zinc ferrite nano-photocatalyst: synthesis, characterization and removal performance, *Spectrosc. Lett.*, 2025, 1–15.

94 A. Saleem, H. Khan, S. M. Bukhari, L. Ben Tahar, U. Farooq and A. J. Shaikh, Lone pair versus aromatic interactions on metal oxide surfaces: a combined spectroscopic and computational study, *Dalton Trans.*, 2025, **54**, 16508–16524.

95 M. Guo, M. Ji and W. Cui, Theoretical investigation of HER/OER/ORR catalytic activity of single atom-decorated graphyne by DFT and comparative DOS analyses, *Appl. Surf. Sci.*, 2022, **592**, 153237.

96 C. Adamo and V. Barone, Toward reliable density functional methods without adjustable parameters: The PBE0 model, *J. Phys. Chem.*, 1999, **110**, 6158–6170.

97 R. A. Burns, J. C. Crittenden, D. W. Hand, V. H. Selzer, L. L. Sutter and S. R. Salman, Effect of inorganic ions in heterogeneous photocatalysis of TCE, *J. Environ. Eng.*, 1999, **125**, 77–85.

98 I. Y. Qudsieh, M. A. Ali and I. M. Maafa, Effect of water matrix on photocatalytic degradation of organic pollutants in water: a literature review, *Rev. Chem. Eng.*, 2025, **41**, 539–573.

99 S. K. Fanourakis, J. Peña-Bahamonde and D. F. Rodrigues, Inorganic salts and organic matter effects on nanorod, nanowire, and nanoplate MoO_3 aggregation, dissolution, and photocatalysis, *Environ. Sci.: Nano*, 2020, **7**, 3794–3804.

100 Y.-H. B. Liao, J. X. Wang, J.-S. Lin, W.-H. Chung, W.-Y. Lin and C.-C. Chen, Synthesis, photocatalytic activities and degradation mechanism of Bi_2WO_6 toward crystal violet dye, *Catal. Today*, 2011, **174**, 148–159.

101 R. Yuan, S. N. Ramjaun, Z. Wang and J. Liu, Photocatalytic degradation and chlorination of azo dye in saline wastewater: kinetics and AOX formation, *Chem.–Eng. J.*, 2012, **192**, 171–178.

102 A. A. Abdel-Khalek, S. Mahmoud and A. Zaki, Visible light assisted photocatalytic degradation of crystal violet, bromophenol blue and eosin Y dyes using AgBr-ZnO nanocomposite, *Environ. Nanotechnol., Monit. Manage.*, 2018, **9**, 164–173.

103 J. Qu, R. Chen, X. Dong and J. He, Effect of NaCl concentrations on the photodecoloration of reactive azo-dyes and their cotton dyeings, *Text. Res. J.*, 2014, **84**, 2140–2148.

104 J. Torres-Luna, R. Ocampo-Pérez, M. Sánchez-Polo, J. R. Utrilla, I. Velo-Gala and L. Bernal-Jacome, Role of HO and SO_4-radicals on the photodegradation of remazol red in aqueous solution, *Chem. Eng. J.*, 2013, **223**, 155–163.

105 N. Kandhasamy, G. Murugadoss, T. Kannappan, K. Kirubaharan, R. K. Manavalan, S. Devanesan, M. S. AlSalhi, R. Mythili, S. Shinde and H. M. Yadav, Synthesis of nickel–manganese sulfide decorated with reduced graphene oxide nanocomposite for ultra-fast photocatalytic degradation of organic dye molecules, *Carbon Lett.*, 2024, **34**, 827–840.

106 M. Saqib, F. Shafiq, W. Qiao, F. Shah and A. M. Khan, Interfacial engineering of Mn-ZnO/g-C_3N_4 heterostructure for selective mixed dye degradation under visible light, *J. Alloys Compd.*, 2026, 187156.

107 S. Karmakar, Particle size distribution and zeta potential based on dynamic light scattering: Techniques to characterize stability and surface charge distribution of charged colloids, Recent Trends Materials, *Chem. Phys.*, 2019, **28**, 117–159.

108 S. K. Azad, M. P. Shah, M. K. Gangwar, P. D. Kunjadia, M. Kumari, F. Ameen and K. S. Prasad, Sorption and subsequent photodegradation of crystal violet dye by CdS and Cu@ CdS prepared using Desulfovibrio vulgaris AU16, *J. Water Proc. Eng.*, 2026, **82**, 109534.

109 J. Naseem, M. A. Rafea, M. E. Zaki, M. I. Attia, M. R. El-Aassar, F. Alresheedi, S. Zulfiqar and M. Aadil, Combining nanotechnology and nanohybrid methods to improve the physical and chemical properties of CuS and boost its photocatalytic aptitude, *RSC Adv.*, 2025, **15**, 13940–13950.

110 S. Kousar, M. A. Rafea, M. E. Zaki, M. Khairy, M. R. El-Aassar, A. K. Alanazi, I. Shakir, S. Mubeen and M. Aadil, Towards advanced remediation: CuS/CdS Z-scheme heterojunction with accelerated charge-transfer for efficient photocatalytic degradation of trypan blue, *RSC Adv.*, 2025, **15**, 39180–39192.

111 M. M. Khalaf, H. M. Abd El-Lateef, M. F. Abou Taleb, H. S. Al Ghamdi and M. Gouda, Fabrication and Mechanistic Insights of an Ag_2O-V_2O_5 Nanocomposite as a Novel Heterojunction Photocatalyst for Efficient Crystal Violet Removal, *J. Indian Chem. Soc.*, 2026, 102548.

112 G. Murugadoss, N. Venkatesh, R. Venkatesan, S.-C. Kim, L. Gnanasekaran and M. Moovendhan, Synergistic enhancement of the photocatalytic and antibacterial activities of cerium and tin-doped zinc sulfide nanoparticles, *Surf. Interfac.*, 2026, 108798.

113 N. Guru Prakash, Z. H. Alhashem, S. V. P. Vattikuti and S. H. Aleithan, Hierarchical In2MnS4 Flower-like Architectures for Efficient Dye Degradation and Methanol Oxidation, *Catalysts*, 2026, **16**, 216.

114 S. C. Shyagathur, A. Hiremath, J. Pattar and H. A. Rao, Visible light harvesting using ZnS/rGO/g-C_3N_4 heterojunction for crystal violet dye degradation: kinetic and mechanistic insights, *Ceram. Int.*, 2025, **52**(2), 1818–1830.

115 M. Z. Ansari and N. Neha, Growth and Characterization of Copper Zinc Tin Sulfide (CZTS), Molybdenum Disulfide (MoS_2) MoS_2, and CZTS/MoS_2 Nanocomposite Photocatalysts for Water Cleaning, *Cureus J.*, 2025, **2**, DOI: 10.7759/s44388-026-00010-z.

116 P. K. Sharma and O. Pandey, Photocatalytic studies of Zn-doped and (Y, Zn)-co-doped CeO_2/CdS heterostructures for the removal of crystal violet dye, *J. Mater. Sci.: Mater. Electron.*, 2022, **33**, 11281–11307.

117 H.-J. Fan, S.-T. Huang, W.-H. Chung, J.-L. Jan, W.-Y. Lin and C.-C. Chen, Degradation pathways of crystal violet by Fenton and Fenton-like systems: condition optimization and intermediate separation and identification, *J. Hazard. Mater.*, 2009, **171**, 1032–1044.

118 W. A. Mohamed, H. A. Mousa, H. H. Abd El-Gawad, H. T. Handal, H. R. Galal, I. A. Ibrahim, S. D. Mekkey, M. A. Ahmed, S. B. Mousa and A. A. Labib, Photophysical effects of TiO_2 quantum dots on phytotoxicity, recycling for solar and photocatalytic processes of industrial effluent, *Results Phys.*, 2023, **46**, 106316.

119 N. Hussain, M. Asif, S. Shafaat, M. S. Khan, N. Riaz, M. Iqbal, A. Javed, T. A. Butt, A. J. Shaikh and M. Bilal, Multilayer adsorption of reactive orange 16 dye onto Fe_2O_3/ZnO hybrid nanoadsorbent: mechanistic insights from kinetics, isotherms and dynamic light scattering studies, *J. Chem. Technol. Biotechnol.*, 2025, **100**, 50–66.